



Radiomanganese PET Detects Changes in Functional β -cell Mass in Mouse Models of Diabetes

Hernandez, Reinier; Graves, Stephen A.; Gregg, Trillian; VanDeusen, Halena R.; Fenske, Rachel J.; Wienkes, Haley N.; England, Christopher G.; Valdovinos, Hector F.; Jeffery, Justin J.; Barnhart, Todd E.; Severin, Gregory; Nickles, Robert J.; Kimple, Michelle E; Merrins, Matthew J.; Cai, Weibo

Published in:
Diabetes

Link to article, DOI:
[10.2337/db16-1285](https://doi.org/10.2337/db16-1285)

Publication date:
2017

Document Version
Peer reviewed version

[Link back to DTU Orbit](#)

Citation (APA):

Hernandez, R., Graves, S. A., Gregg, T., VanDeusen, H. R., Fenske, R. J., Wienkes, H. N., ... Cai, W. (2017). Radiomanganese PET Detects Changes in Functional β -cell Mass in Mouse Models of Diabetes. *Diabetes*, 66(8), 2163-2174. DOI: 10.2337/db16-1285

General rights

Copyright and moral rights for the publications made accessible in the public portal are retained by the authors and/or other copyright owners and it is a condition of accessing publications that users recognise and abide by the legal requirements associated with these rights.

- Users may download and print one copy of any publication from the public portal for the purpose of private study or research.
- You may not further distribute the material or use it for any profit-making activity or commercial gain
- You may freely distribute the URL identifying the publication in the public portal

If you believe that this document breaches copyright please contact us providing details, and we will remove access to the work immediately and investigate your claim.

Radiomanganese PET Detects Changes in Functional β -cell Mass in Mouse Models of Diabetes

Reinier Hernandez,¹ Stephen A. Graves,¹ Trillian Gregg,^{2,3} Halena R. VanDeusen,² Rachel J. Fenske,² Haley N. Wienkes,² Christopher G. England,¹ Hector F. Valdovinos,¹ Justin J. Jeffery,⁴ Todd. E Barnhart,¹ Gregory W. Severin,^{5,6} Robert J. Nickles,¹ Michelle E. Kimple,^{2,7} Matthew J. Merrins,^{2,7,8} and Weibo Cai^{1,4,9}

¹Department of Medical Physics, University of Wisconsin-Madison, Madison, WI, USA, ²Department of Medicine, Division of Endocrinology, Diabetes & Metabolism, University of Wisconsin-Madison, Madison, WI, USA, ³Program in Biophysics, University of Wisconsin-Madison, Madison, WI, USA, ⁴Carbone Cancer Center, University of Wisconsin-Madison, Madison, WI, USA, ⁵Center for Nuclear Technologies, Technical University of Denmark, 4000 Roskilde, Denmark, ⁶Department of Chemistry, Michigan State University, East Lansing, MI, USA, ⁷William S. Middleton Memorial Veterans Hospital, Madison, WI, USA, ⁸Department of Biomolecular Chemistry, University of Wisconsin-Madison, Madison, WI, USA, ⁹Department of Radiology, University of Wisconsin-Madison, Madison, WI, USA.

Corresponding authors: Matthew J. Merrins; C4134A VA Hospital, Madison, WI 53705; email: merrins@wisc.edu; phone: (716) 397-7557
and Weibo Cai, 1111 Highland Ave WIMR 7137, Madison, WI 53705; email: wcai@uwhealth.org; phone: (608) 262-1749

Short title: $^{52}\text{Mn}^{2+}$ -PET imaging of functional β -cell mass

Authorship note: R.H. and S.A.G. contributed equally to this work.

The noninvasive measurement of functional β -cell mass would be clinically valuable for monitoring the progression of type 1 and type 2 diabetes, as well as the viability of transplanted insulin-producing cells. Although previous work employing magnetic resonance imaging has shown promise for functional β -cell mass determination through voltage-dependent Ca^{2+} channel (VDCC)-mediated internalization of Mn^{2+} , the clinical utility of this technique is limited by the cytotoxic levels of Mn^{2+} contrast agent. Here, we show that positron emission tomography (PET) is advantageous for determining functional β -cell mass using $^{52}\text{Mn}^{2+}$ ($t_{1/2}$: 5.6 d). We investigated the whole-body distribution of $^{52}\text{Mn}^{2+}$ in healthy adult mice by dynamic and static PET imaging. Pancreatic VDCC uptake of $^{52}\text{Mn}^{2+}$ was successfully manipulated pharmacologically *in vitro* and *in vivo* using glucose, nifedipine (VDCC blocker), the sulfonylureas tolbutamide and glibenclamide (K_{ATP} channel blockers), and diazoxide (K_{ATP} channel opener). In a mouse model of streptozotocin (STZ)-induced type 1 diabetes, $^{52}\text{Mn}^{2+}$ uptake in the pancreas was distinguished from healthy controls in parallel with classic histological quantification of β -cell mass from pancreatic sections. $^{52}\text{Mn}^{2+}$ -PET also reported the expected increase in functional β -cell mass in the *ob/ob* model of pre-type 2 diabetes, a result corroborated by histological β -cell mass measurements and live-cell imaging of β -cell Ca^{2+} oscillations. These results indicate that $^{52}\text{Mn}^{2+}$ -PET is a sensitive new tool for the non-invasive assessment of functional β -cell mass.

Type 1 and type 2 diabetes, while arising from different etiologies, are each associated with the functional loss of insulin-secreting β -cells and can lead to life-threatening complications such as cardiovascular disease and neuropathy (1). As such, a variety of therapeutics are being pursued that aim to preserve, expand, or replace β -cells. An imaging modality capable of monitoring functional β -cell mass *in vivo* as well as the viability of islet- or stem cell-derived β -cell transplants would therefore be invaluable to future therapeutic investigations.

Human pancreatic islets occupy approximately 4.5% of the pancreas volume, and are composed of a mixture of β , α , γ , δ , and ϵ cells (2; 3). As individual islets vary in size from 25 to 400 μm in diameter (3-5) and are non-uniformly distributed throughout the pancreas, quantification is challenging through noninvasive anatomical imaging techniques such as magnetic resonance imaging (MRI) or computed tomography (CT) (6). Alternatively, positron emission tomography (PET) is a technique that involves quantifying the *in vivo* distribution of a biologically relevant moiety by tracking a positron-emitting radioisotope. Compared with MRI and CT, PET has significantly greater imaging sensitivity and inherently probes physiology rather than anatomy (7), which may prove useful in the clinical quantification of functional β -cell mass.

Mn^{2+} , in a behavior that mimics Ca^{2+} , is freely transported through voltage-dependent Ca^{2+} channels (VDCC) (8; 9). Since VDCC activation is required for the release of insulin from β -cells, Mn^{2+} has been proposed as a molecular imaging agent for probing β -cell function and mass using Mn^{2+} -enhanced magnetic resonance imaging (MEMRI) (10-15). However, this technique is limited by significant cellular toxicity and the slow biological clearance of Mn^{2+} , which prevents the possibility of repeated administration (9; 16). Since PET has several orders of magnitude higher sensitivity than MRI, the objective of this work was to assess the feasibility of using PET to probe β -cell mass and function.

Herein, we take advantage of the exceptional sensitivity and quantitation capability of PET and the availability of radiomanganese ($^{52}Mn^{2+}$) to noninvasively image functional β -cell mass *in vivo*. When intravenously injected in mice, $^{52}Mn^{2+}$ ($t_{1/2}$: 5.6 d) showed a rapid accumulation in the mouse pancreas that was sensitive to glucose and pharmacologic manipulation of VDCC. We also explored the potential of $^{52}Mn^{2+}$ -PET to detect changes in functional β -cell mass in mouse models of type 1 and type 2 diabetes. Overall, our results point to the significant potential for radiomanganese to overcome several limitations of other β -cell imaging agents and potentially become a method of choice for studying β -cell physiology noninvasively.

RESEARCH DESIGN AND METHODS

$^{52}Mn^{2+}$ -PET Imaging

Aliquots of the buffered $^{52}Mn^{2+}$ solution (0.01M NaOAc, pH 6.5) were diluted to the desired injection volume (~200 μ l) with phosphate-buffered saline (PBS), typically 2 – 4 MBq (approximately 50 – 100 μ Ci) per subject. The acquisition of PET images was performed with an Inveon μ PET/ μ CT scanner (Siemens Preclinical Solutions). To study the biodistribution and clearance of $^{52}Mn^{2+}$ in the mouse, 3.7 MBq (100 μ Ci) of $^{52}Mn^{2+}$ was IV injected into female ICR mice. Due to the long decay half-life of ^{52}Mn ($t_{1/2}$: 5.6 d), PET scans were recorded at multiple time-points between 1 h and 13 days post-injection of the radiotracer. Before each scan, mice were anesthetized with isoflurane (4% induction; 1%

maintenance) and placed in the scanner in the prone position. $30\text{--}40 \times 10^6$ coincidence events per mouse static PET scans were acquired (time window, 3.432 ns; energy window, 350–650 keV) and the PET images were reconstructed in Inveon Acquisition Workplace (Siemens Preclinical Solutions) workstation using a non-scatter-corrected three-dimensional Ordered Subset Expectation Optimization/Maximum a Posteriori (OSEM3D/MAP) algorithm. Region-of-interest (ROI) analysis was performed after organs were manually delineated on the PET images. Tissue $^{52}\text{Mn}^{2+}$ uptake values are reported as standardized uptake value (SUV), which is normalized to whole body radiomanganese concentration to account for weight disparities between animal models. Percentage injected dose per gram of tissue (%ID/g) is also reported in the Supplementary Material (**Table S6-S9**). To acquire dynamic PET scans, mice were anesthetized with isoflurane and the lateral tail vein was catheterized. Simultaneous with the administration of approximately 1.7 MBq ($\sim 50 \mu\text{Ci}$) of $^{52}\text{Mn}^{2+}$ as a fast IV bolus, one-hour scans were recorded and list-mode files were binned into 46 frames (12 \times 5 s, 6 \times 10 s, 6 \times 30 s, 10 \times 60 s, 6 \times 150 s, 6 \times 300 s) and the images reconstructed using the OSEM3D/MAP algorithm. For comparison, 1.7 MBq (50 μCi) of $^{52}\text{Mn}^{2+}$ was continuously infused with a syringe pump (KD Scientific, Model 780100) during the first 30 min of a 60 min experiment, and list-mode files were binned into 30 frames (2 min each) and reconstructed using the OSEM3D/MAP algorithm.

Effect of Pharmacological VDCC Manipulation on $^{52}\text{Mn}^{2+}$ Uptake In Vivo

Pancreatic $^{52}\text{Mn}^{2+}$ uptake was stimulated using glucose and glibenclamide (Tocris Biosciences), which is known to promote insulin release in β -cells via blockade of ATP-sensitive K^+ channels (K_{ATP}). Mice were injected IP with 100 μL of 1 g/kg glucose, or glucose plus 5 mg/kg glibenclamide in PBS, 15 min before the IV injection of 0.74 – 1.85 MBq (20 – 50 μCi) of $^{52}\text{Mn}^{2+}$. VDCC blockade was achieved via IP injection of 20 mg/kg nifedipine (MP Biomedicals) dissolved in dimethyl sulfoxide. To activate K_{ATP} channels, mice received an IP injection of 20 mg/kg diazoxide (Tocris Biosciences) in PBS, a clinically used K_{ATP} agonist, 15 min before injection of 0.74 MBq (20 μCi) of $^{52}\text{Mn}^{2+}$. Whole-body PET scans were

acquired 1 h after the injection of the radiotracer, after which *ex vivo* biodistribution analysis was performed.

$^{52}\text{Mn}^{2+}$ -PET Studies in a Type 1 Diabetes Model

Type 1 diabetes was induced in female ICR mice via a single IP injection of 180 mg/kg streptozotocin (STZ; MP Biomedical), a toxin that selectively destroys pancreatic β -cells (17). The injectable STZ solution (12.5 mg/mL) was prepared fresh in PBS. The weight of each mouse was measured daily, and blood glucose levels were recorded every other day with a glucometer (TRUEresult, Trividia Health Inc.) using blood samples collected from the tail vein. Mice were considered diabetic after two consecutive blood glucose readings above 250 mg/dL and were used for $^{52}\text{Mn}^{2+}$ -PET imaging studies one week after the injection of STZ. To evaluate $^{52}\text{Mn}^{2+}$ pancreatic uptake on diabetic mice, 0.74 MBq (20 μCi) of radioactivity was administered IV and static PET images were recorded 1 h after administration of the tracer. *Ex vivo* biodistribution was carried out following PET acquisition.

$^{52}\text{Mn}^{2+}$ -PET Studies in a Pre-Type 2 Diabetes Model

Pancreatic uptake of $^{52}\text{Mn}^{2+}$ in was measured in 10-week-old wildtype and *ob/ob* mice on the C57BL/6J background. For PET imaging, 0.74 MBq (20 μCi) of $^{52}\text{Mn}^{2+}$ was IV injected 1 h prior to PET scan acquisition. $^{52}\text{Mn}^{2+}$ accumulation in the pancreas and other organs of interest was also quantified by *ex vivo* biodistribution analysis.

Additional Materials and Methods

Animal studies were conducted under the approval of UW Institutional Animal Care and Use Committee. Detailed information on animal models, isotope production, *ex vivo* biodistribution, islet isolation and imaging, and β -cell mass measurement is provided as supplementary information.

RESULTS

In vivo whole-body PET and biodistribution of $^{52}\text{Mn}^{2+}$ in normal mice

The *in vivo* biodistribution of $^{52}\text{Mn}^{2+}$ was investigated noninvasively with PET and *ex vivo* gamma counting. **Figure 1A** shows coronal planes intersecting the pancreas of ICR mice, in PET scans acquired between 1 hour and 13 days after IV injection of 3.7 MBq (100 μCi) of $^{52}\text{Mn}^{2+}$. A rapid and prominent accumulation of $^{52}\text{Mn}^{2+}$ was observed in the pancreas, kidneys, liver, heart, and salivary glands (5.13 ± 0.38 , 5.13 ± 0.02 , 3.27 ± 0.36 , 2.11 ± 0.20 , and 2.30 ± 0.26 SUV at 1 h post-injection, respectively; $n=3$; **Figure 1B**). In the subsequent time points during the longitudinal study, $^{52}\text{Mn}^{2+}$ uptake gradually declined in all organs except the salivary gland where uptake remained stable at a SUV of ~ 3 (**Figure 1B, Table S1**). $^{52}\text{Mn}^{2+}$ uptake in the pancreas, which was highest at 1 h post-injection, was notably higher than that in the liver and kidneys at all time points. Such favorable pancreas-to-normal organ contrast ratios, which peaked at about 3 days after $^{52}\text{Mn}^{2+}$ administration, facilitated an easy delineation of the pancreas (**Figure S1**). Uptake in the muscle was very low and had little variation during the study. *Ex vivo* biodistribution was performed after the last PET scan 13 days post-injection, confirming a marked accumulation of $^{52}\text{Mn}^{2+}$ in the salivary gland, pancreas, kidneys, and to a lesser extent, the heart and liver (**Figure 1C, Table S2**). Other organs including the brain, lungs, bones, intestines, stomach, and spleen displayed low $^{52}\text{Mn}^{2+}$ uptake, typically less than 0.5 SUV.

Because the whole-body distribution of $^{52}\text{Mn}^{2+}$ occurred largely within the first hour after IV administration (**Figure 1**), a dynamic PET study was designed to investigate the $^{52}\text{Mn}^{2+}$ kinetics during this time. **Figure 2** shows the time-activity curves (TACs) resulting from ROI analysis of the dynamic PET data corresponding to the pancreas, liver, kidneys, heart, salivary gland, and muscle under two IV administration regimes: rapid bolus injection, and 30 min continuous infusion. The analysis of the myocardial TAC revealed extremely fast blood extraction kinetics with a blood circulation half-life of 10.7 ± 3.5 s in mice administered a rapid IV $^{52}\text{Mn}^{2+}$ bolus. Consequently, $^{52}\text{Mn}^{2+}$ uptake was stabilized in the organs of interests within 5 min post-injection. A residual radioactivity of 2.60 ± 0.41 SUV was observed in the heart at 1 h post-injection, which was consistent with the specific uptake of Mn^{2+} ions by myocardial tissue. Compared to the static 1 h post-injection PET scans (**Figure 1**), similar $^{52}\text{Mn}^{2+}$ uptake

values were observed following rapid bolus injection in the heart (2.11 ± 0.20 vs. 2.60 ± 0.41 SUV) and muscle (0.38 ± 0.03 vs 0.16 ± 0.02 SUV), while liver (3.27 ± 0.34 vs. 5.16 ± 1.46 SUV) and kidneys (5.13 ± 0.02 vs. 7.81 ± 0.51 SUV) were much higher at the end of the dynamic scan after a rapid IV $^{52}\text{Mn}^{2+}$ bolus. Interestingly, a ~50% reduction in pancreatic uptake from 5.13 ± 0.38 to 2.74 ± 0.59 SUV was observed in the dynamic studies.

As clearly depicted in **Figure 2** (red curves), continuous infusion of $^{52}\text{Mn}^{2+}$ over a 30-min time period resulted in a linear ramping in organ radioactivity, followed by an immediate plateau upon infusion termination that persisted for the remainder of the experiment. This method highlights the rapid distribution kinetics of $^{52}\text{Mn}^{2+}$ and the comparable results obtained by either rapid bolus or continuous infusion of $^{52}\text{Mn}^{2+}$. Only the kidney displayed higher radioactivity at 1 h post-injection in mice administered the rapid bolus vs. mice receiving continuous $^{52}\text{Mn}^{2+}$ infusion, 7.81 ± 0.51 vs. 5.14 ± 1.21 SUV, respectively (n=4). During the continuous infusion regime, pancreas reached an uptake of 3.44 ± 0.69 SUV which, similar to the rapid bolus injection, was also significantly lower than that in the static PET scans at 1 h post-injection (5.13 ± 0.38 SUV).

Previous reports have shown that many volatile anesthetics, including isoflurane, impair insulin secretion by inhibiting the glucose-dependent inactivation of K_{ATP} channels (18; 19). Plausibly, the observed decrease in pancreatic uptake of $^{52}\text{Mn}^{2+}$ resulted from mice being anesthetized through the full extent of the studies during the dynamic PET scans. To investigate the impact of isoflurane anesthesia on pancreatic uptake of $^{52}\text{Mn}^{2+}$, 1 h post-injection biodistribution experiments were performed under different administration conditions in either anesthetized (1% isoflurane) or awake mice. **Figure S2** shows that isoflurane significantly inhibited the accumulation of $^{52}\text{Mn}^{2+}$ in the pancreas regardless of the administration regime (rapid bolus vs infusion) or glucose stimulation, suggesting that isoflurane indeed acts as an indirect VDCC inhibitor upstream of K_{ATP} channel closure.

Uptake of $^{52}\text{Mn}^{2+}$ in isolated islets

To corroborate the mechanism of $^{52}\text{Mn}^{2+}$ uptake in the pancreas and its dependence on VDCC, an *ex vivo* $^{52}\text{Mn}^{2+}$ uptake study was performed in islets isolated from *ob/ob* mice (to take advantage of the 2-fold greater islet yield vs. wildtype mice). Due to the similarities between Mn^{2+} and Ca^{2+} ions, Mn^{2+} uptake by β -cells occurs via influx through VDCC (**Figure 3A**) (20; 21). Isolated islets were incubated with 0.37 MBq (10 μCi) of $^{52}\text{Mn}^{2+}$ under several conditions that stimulate/inhibit VDCC (**Figure 3B**). $^{52}\text{Mn}^{2+}$ was readily taken up by islets, even in the presence of low (1 mM) glucose, as expected for the high basal Ca^{2+} and insulin secretion reported for *ob/ob* β -cells (22). $^{52}\text{Mn}^{2+}$ uptake was significantly enhanced ($P < 0.05$) when the islets were stimulated with 10 mM glucose. Importantly, $^{52}\text{Mn}^{2+}$ uptake was completely blocked by the further application of diazoxide (50 μM), which inhibits the opening of VDCC via activation of K_{ATP} channels. As expected for the clearance of intracellular Ca^{2+} in response to diazoxide (23), intracellular $^{52}\text{Mn}^{2+}$ fell below the basal level. Conversely, glucose administered with the K_{ATP} channel blocker tolbutamide (250 μM) resulted in significantly higher $^{52}\text{Mn}^{2+}$ retention than glucose alone. Taken together, these experiments demonstrate that pancreatic islet uptake of $^{52}\text{Mn}^{2+}$ depends on the activity of β -cell VDCC.

Pharmacological manipulation of $^{52}\text{Mn}^{2+}$ pancreatic uptake *in vivo*

To verify the specificity of $^{52}\text{Mn}^{2+}$ accretion in the pancreas noninvasively using PET imaging, $^{52}\text{Mn}^{2+}$ pancreatic uptake was pharmacologically manipulated *in vivo* through the inhibition or stimulation of VDCC. In line with the *in vitro* results, inhibition of VDCC by direct blockade with nifedipine, or activation of K_{ATP} with diazoxide resulted in a significant ($P < 0.0001$) abrogation of the PET signal within the pancreas. **Figure 4A** shows coronal PET slices of the pancreas of ICR mice receiving 20 mg/kg IP injections of nifedipine or diazoxide, 10-15 min before the administration of an intravenous $^{52}\text{Mn}^{2+}$ bolus. Compared to the control group, a clear decrease in pancreatic PET signal was observed 1 h following injection of $^{52}\text{Mn}^{2+}$. PET quantification revealed a 44% (5.13 ± 0.36 vs. 2.85 ± 0.92 SUV) and 54% (5.13 ± 0.36 vs. 2.36 ± 0.61 SUV) decline in $^{52}\text{Mn}^{2+}$ uptake in groups administered diazoxide and nifedipine, respectively (**Figure 4B and C**). The remnant pancreatic signal suggests that IP drug injection

of resulted in the incomplete blockade of VDCC, or more likely, that some $^{52}\text{Mn}^{2+}$ uptake is independent of VDCC (8). On the contrary, mice administered glibenclamide (5 mg/kg) exhibited a significant enhancement in pancreatic uptake of $^{52}\text{Mn}^{2+}$. The distribution of $^{52}\text{Mn}^{2+}$ in other organs of interest including the heart, liver, kidneys, spleen and salivary gland remained largely unaltered among groups (**Table S3 and S4**). These results demonstrate the potential of $^{52}\text{Mn}^{2+}$ PET imaging to noninvasively detect changes in functional β -cell mass.

$^{52}\text{Mn}^{2+}$ uptake in mouse models of type 1 and type 2 diabetes

We further investigated the correlation between pancreatic $^{52}\text{Mn}^{2+}$ uptake and functional β -cell mass in a murine model of type 1 diabetes. Diabetes was induced in female ICR mice via a single streptozotocin (STZ) injection (180 mg/kg). Four days after injection (**Figure 5A**), mice presented signs of hyperglycemia (blood glucose > 250 mg/dL) and weight loss that indicated a diabetic status. As seen in the PET images (**Figure 5B**), $^{52}\text{Mn}^{2+}$ accumulation within the pancreas of diabetic mice was reduced by ~60%, from 5.13 ± 0.38 SUV (n=3) in normal mice to 2.04 ± 0.81 SUV (n=3) in diabetic mice ($P < 0.0001$) (**Figure 5C, Table S3 and S4**). *Ex vivo* biodistribution analysis corroborated a very similar (58%) decrease in pancreatic accumulation of $^{52}\text{Mn}^{2+}$ (**Figure 5D**). To compare $^{52}\text{Mn}^{2+}$ -PET imaging with a direct histological assessment of β -cell mass, 3 pancreata per treatment group were weighed, sectioned, and immunostained for insulin. On average, β -cell mass in the STZ-treated mice fell by ~70% when compared to the sham-injected ICR mice (**Figure 5E**), in good agreement with the $^{52}\text{Mn}^{2+}$ PET data.

$^{52}\text{Mn}^{2+}$ -PET imaging studies were also performed in C57BL/6J mice carrying the *lep^{ob}* (*ob/ob*) spontaneous mutation that results in obesity and pre-type 2 diabetes. In this case, $^{52}\text{Mn}^{2+}$ accumulation in the pancreas of *ob/ob* mice was significantly ($P < 0.001$) higher than the wildtype C57BL/6J mice (**Figure 6A**). 1 h after administration of $^{52}\text{Mn}^{2+}$ (n=3), pancreatic uptake was 4.89 ± 0.68 SUV in wildtype C57BL/6J mice and 7.27 ± 1.03 SUV in *ob/ob* mice (**Figure 6B**). *Ex vivo* biodistribution analysis corroborated the statistically significant differences in pancreatic SUV between the groups ($P < 0.001$; **Figure S3 and Table S5**). Uptake in the liver and salivary gland was very similar in *ob/ob* and wildtype

animals with SUVs of 3.68 ± 0.25 vs. 3.40 ± 0.73 and 3.11 ± 1.05 vs. 2.40 ± 0.20 , respectively. In agreement with $^{52}\text{Mn}^{2+}$ -PET imaging, *post hoc* analysis of insulin-stained pancreatic sections showed a significantly ($P < 0.05$, $n=3$) increased β -cell mass in *ob/ob* mice relative to controls (**Figure 6C**). We also observed that *ob/ob* islet Ca^{2+} levels, which oscillate in response to glucose stimulation (**Figure 6D**), were strongly left-shifted in their glucose dependence relative to controls (**Figures 6E, 6F**), in agreement with the *in vivo* $^{52}\text{Mn}^{2+}$ -PET results and prior functional studies (22). Notably, in contrast to the experiments in **Figure 4**, where pharmacologic VDCC manipulation was used to strictly define functional β -cell mass, the experiments in **Figures 5 and 6** show that basal $^{52}\text{Mn}^{2+}$ uptake (measured in the absence of exogenous glucose or VDCC inhibitors) remains heavily dependent on changes in β -cell mass. Both approaches, when applied clinically, are likely to yield useful information.

DISCUSSION

The loss of functional β -cell mass is a cornerstone of both type 1 and type 2 diabetes (24). Here, we leverage the ability of β -cells to sequester divalent metal ions (e.g. Ca^{2+} , Mn^{2+} , Zn^{2+} , and Co^{2+}), which is essential to the production and release of insulin. While β -cell function has been widely investigated based on the measurement of Ca^{2+} currents *in vitro* (25), little progress has been achieved in exploring divalent metal intake for measurement of functional β -cell mass *in vivo*. Part of this is due to the lack of effective methods to track the distribution of most of these metals. Fortunately, $^{52}\text{Mn}^{2+}$ has both magnetic and nuclear properties that facilitate its noninvasive detection by MRI, and with greater sensitivity, PET. In the present work, we report the use of radioactive manganese for noninvasive PET imaging of the mouse pancreas. When injected intravenously, $^{52}\text{Mn}^{2+}$ accumulated significantly into pancreatic tissue with exceptionally fast blood extraction kinetics. $^{52}\text{Mn}^{2+}$ uptake in the pancreas, which peaked within minutes following administration in healthy mice, was on the order of 5-6 SUV with slow clearance half-life of approximately 8 days. Our results demonstrate that *in vivo* measurements of functional β -cell mass by $^{52}\text{Mn}^{2+}$ -PET offers complementary information to existing β -cell function assays that lack spatial

information (e.g. measurement of c-peptide release), as well as measures of β -cell mass that cannot predict β -cell function (e.g. PET imaging with radiolabeled exendin-4).

A key finding of our work was that 50-60% of the observed pancreatic radioactivity resulted from the specific uptake of $^{52}\text{Mn}^{2+}$ through VDCC, implicating β -cells. By pharmacologically manipulating the mechanism of VDCC in isolated islets, we were able to correlate the uptake of radioactive $^{52}\text{Mn}^{2+}$ with Ca^{2+} uptake. This agrees with other *in vitro* studies using non-radioactive Mn^{2+} that reported a correlation between Mn^{2+} uptake and changes in β -cell functional capacity arising from the triggering pathway (14; 15; 26). Similarly, *in vivo* studies demonstrated that chemical inhibition of VDCC, using nifedipine or diazoxide, resulted in a drastic decline in the accumulation of $^{52}\text{Mn}^{2+}$ within the pancreas. In addition, the stimulation of VDCC with glucose and glibenclamide led to an increase in $^{52}\text{Mn}^{2+}$ uptake in the pancreas. Overall, our results indicated that the $^{52}\text{Mn}^{2+}$ uptake observed in the pancreas was largely mediated by and dependent on the functional β -cell mass, keeping in mind that $^{52}\text{Mn}^{2+}$ -PET would be blind to defects in the neurohormonal amplifying pathways of insulin secretion, which are largely VDCC-independent (27).

Our next question was if this method was sensitive enough to detect changes in functional β -cell mass that occur during diabetes progression and disease. First, we employed an experimental animal model of STZ-induced type 1 diabetes, which showed a ~60% reduction in the pancreatic accumulation of $^{52}\text{Mn}^{2+}$, while uptake in other organs remained unaltered. Direct measurements of β -cell mass by histology showed a comparable decline (~70%), indicating the capability of $^{52}\text{Mn}^{2+}$ -PET imaging for revealing extreme cases of β -cell loss. Equally relevant results were observed in the obese mouse (*ob/ob*) model of pre-type 2 diabetes, where significant ($P < 0.0001$) enhancement in pancreatic uptake of $^{52}\text{Mn}^{2+}$ was observed. These results agree with previous reports showing that *ob/ob* mice do not progress to type 2 diabetes (28; 29), but rather present markedly higher functional β -cell mass compared with wildtype mice at 10 weeks of age, as assessed by histology and live-cell Ca^{2+} imaging. Probing the gradual gain/loss of functional β -cell mass using $^{52}\text{Mn}^{2+}$ ($t_{1/2} = 5.6$ d) was not feasible due to its long radioactive half-life. Rather than trying to account for the remnant ^{52}Mn radioactivity in the pancreas,

longitudinal studies would benefit from the use of the shorter-lived ^{51}Mn ($t_{1/2}$: 45.6 min), which would facilitate regular monitoring of variations in functional β -cell mass without the interference of remnant radioactivity. This is the subject of our future work.

As there can be significant changes in β -cell function long before changes in anatomical mass are observed (30-32), it is advantageous that the relative uptake of $^{52/51}\text{Mn}^{2+}$ *in vivo* depends on the functional β -cell mass. This ability has the potential to shed light on the rate of functional β -cell mass decline in asymptomatic type 1 diabetic patients, as well as the survival of β -cell transplants, including stem cell-derived β -cells. Whether $^{51/52}\text{Mn}^{2+}$ -PET is capable of measuring very subtle changes in this parameter is the pivotal question to its clinical significance. The diffusion of Mn^{2+} through β -cell VDCCs depends on their activation by glucose or drug-based stimulation. This has been shown here through *in vitro* and *in vivo* functional suppression and enhancement studies. For a given state of glucose activation, the amount of Mn^{2+} cellular internalization by the pancreas is partly controlled by the number of available VDCCs, which should be proportional to functional β -cell mass. However, accurate quantification of functional β -cell mass will require subtraction of nonspecific exocrine pancreas uptake of the radiotracer. For this reason, the $^{52}\text{Mn}^{2+}$ -PET measurements in *ob/ob* mice underestimate the predicted effect on functional β -cell mass. Calibration may be accomplished through pharmacological manipulation to acutely suppress VDCC-mediated uptake of $^{52}\text{Mn}^{2+}$ using nifedipine, diazoxide, or other suppressing agents. Though, same subject calibration will require the implementation of either back-to-back PET scans using the shorter-lived $^{51}\text{Mn}^{2+}$, or the performance of dynamic PET scanning under a $^{52}\text{Mn}^{2+}$ infusion regime that allows for the deconvolution of the endocrine signal from the exocrine background.

Aside from VDCC, there are several endogenous mechanisms for Mn^{2+} uptake including facilitated diffusion, divalent metal transporter-1 (DMT1), Zrt and Irt-related protein-8 (ZIP-8), transferrin receptor (TfR), and ionotropic glutamate receptor Ca^{2+} channels (8). The relative role that these alternative pathways play in $^{52}\text{Mn}^{2+}$ transport remains unknown, but a lack of impact by nifedipine suggests that VDCC may not be a primary transport route in many normal tissues. In this regard, our

studies also provided valuable information on the kinetics of the whole-body distribution of $^{52}\text{Mn}^{2+}$. Besides the pancreas, $^{52}\text{Mn}^{2+}$ also accumulated in the liver, heart, kidneys, and salivary gland. Despite the significant kidney uptake, no clear sign of renal excretion was observed and most of the $^{52}\text{Mn}^{2+}$ clearance occurred through the hepatobiliary system. From the analysis of the image-derived dynamic TAC of the heart, we estimated a $^{52}\text{Mn}^{2+}$ circulation half-life of 10.7 ± 3.5 s following a rapid bolus injection, which aligned with previous studies showing an extremely fast (~ 0.8 min) blood clearance of ^{54}Mn in dogs (33). Such fast extraction kinetics indicate that compartmental modeling could be used to describe $^{52}\text{Mn}^{2+}$ uptake in a more quantitative manner. A stable residual myocardial uptake was observed after complete blood clearance, approximately 1 min after injection. Of note was the marked underestimation of myocardial uptake by PET compared to biodistribution results, with an average recovery coefficient of 0.54. This is an inherent limitation of the PET imaging-based quantification of small volumes such as the myocardial wall or adrenal glands, which in mice are affected by significant partial volume effects (34; 35).

Several PET tracers have been studied as potential β -cell imaging agents. [^{11}C]-Dihydropyridazine (DTPZ) and the ^{18}F -labeled DTPZ analog FP-(+)-DTPZ have been shown to have high affinity for the type 2 vesicular acetylcholine transporter (VMAT2), which is expressed on the surface of rodent β -cells but appears to be entirely absent from pancreatic exocrine tissue (36-39). Unfortunately, primate models have shown very low pancreatic uptake of [^{11}C]-DTPZ, which suggests that the degree of VMAT2 expression is species-dependent (40-42). More work is needed in quantifying human β -cell expression of VMAT2, and how expression density is related to β -cell function. Another promising PET approach for monitoring *in vivo* β -cell mass involves compartmental kinetic analysis of [^{11}C]-5-HTP, a compound used clinically for detection of neuroendocrine tumors (43). This compound has shown differential clearance from endocrine vs. exocrine pancreatic tissues based on differences in the presence of serotonin biosynthesis machinery, which effect [^{11}C]-5-HTP retention in endocrine cells. With this approach, [^{11}C]-5-HTP tracer uptake is observed to decrease both longitudinally in patients with type 2

diabetes and cross-sectionally in patients with type 1 diabetes when compared with healthy controls (44; 45). Another category of tracers includes radiolabeled (e.g. ^{18}F , ^{68}Ga , ^{64}Cu , ^{111}In) derivatives of exendin-4, a glucagon-like protein-1 receptor (GLP-1R) agonist (46-50). Fluorescence microscopy has shown that GLP-1R is only located on β -cells within the human pancreas (51), making it an attractive molecular imaging target due to its specificity. In animals models, exendin-4-PET suffers from low pancreatic uptake relative to the surrounding organs (<0.3 %ID/g in Sprague-Dawley rats at 1 h post-injection whereas proximal kidney uptake is >25 %ID/g) (52). Although the kidney uptake of $^{52}\text{Mn}^{2+}$ is also significant, the pancreatic uptake of $^{52}\text{Mn}^{2+}$ is comparatively high such that improved pancreas-to-background ratios are attained by $^{52}\text{Mn}^{2+}$ -PET. In general, the implementation of tracers targeting surface receptors of β -cells is extremely challenging, considering the low total mass of β -cells, diffuse pancreatic distribution, and heterogeneous receptor expression.

Aside from following the gain/loss of β -cell mass in pre-diabetic/diabetic patients, there is a pressing need for a noninvasive method for longitudinal imaging of β -cell transplants. Islet transplantation has been shown to lead to temporary insulin independence in patients with type 1 diabetes (53; 54), but has not been widely adopted due to the need for donor tissues. Recent advances in selective stem cell differentiation techniques will likely lead to wider clinical adoption of β -cell transplantation therapies (55). The ability to noninvasively track the survival and function of transplanted β -cells would enable research into the patient-specific efficacy assessment of immune-modulating therapies and the development of new therapeutic strategies (56). In this case, the use of ^{51}Mn -PET for monitoring islet transplant survival is compelling, since it can be performed repeatedly and safely over time.

In conclusion, the prominent pancreatic uptake, rapid localization kinetics, and well characterized metabolic pathways of $^{52}\text{Mn}^{2+}$ make it a promising agent for noninvasive PET imaging of functional β -cell mass, and was corroborated by various *post hoc* experiments such as histological β -cell mass measurements and live-cell imaging of β -cell Ca^{2+} oscillations. With further development, $^{51}\text{Mn}^{2+}$ PET may also find broad applications in venues ranging from basic research to clinical patient care.

AUTHOR CONTRIBUTIONS

R.H. and S.A.G. conceived the project, performed preparatory experimentation and method development, collected and analyzed data, and prepared the manuscript. T.G. contributed to the experimental design and assisted with the *ex vivo* $^{52}\text{Mn}^{2+}$ -PET experiments. H.R.V. performed the Ca^{2+} imaging studies. R.J.F and H.N.W. performed the β -cell mass measurements. C.G.E. and J.J.J. assisted with PET image acquisition, *ex vivo* biodistribution studies, and data analysis. G.W.S., H.F.V., and T.E.B. developed radioisotope production tools, assisted with tracer quality assurance, and contributed to experimental design. R.J.N, M.E.K., M.J.M, and W.C. supervised project execution, provided technical support, assisted with data interpretation, and edited the manuscript. M.J.M. and W.C. are the guarantors of this work and, as such, had full access to all the data in the study and take responsibility for the integrity of the data and the accuracy of the data analysis.

ACKNOWLEDGEMENTS

The Merrins laboratory gratefully acknowledges support from the American Diabetes Association (1-16-IBS-212, 1-17-PDF-155), the NIH/NIDDK (K01DK101683), the NIH/NIA (R21AG050135), and the University of Wisconsin-Madison School of Medicine and Public Health Wisconsin Partnership Program. The Cai laboratory gratefully acknowledges support from the University of Wisconsin-Madison, the National Science Foundation (DGE-1256259), and the National Institutes of Health (NIBIB/NCI 1R01CA169365, 1R01EB021336, P30CA014520, T32-CA009206, and T32-GM008349). We are also grateful to Dr. James Holden for sharing his expertise in the experimental design and dynamic PET modeling. Authors declare no conflict of interest.

REFERENCES

1. Forbes JM, Cooper ME: Mechanisms of diabetic complications. *Physiol Rev* 2013;93:137-188
2. Ionescu-Tirgoviste C, Gagniuic PA, Gubceac E, Mardare L, Popescu I, Dima S, Militaru M: A 3D map of the islet routes throughout the healthy human pancreas. *Sci Rep* 2015;5:14634
3. Kim A, Miller K, Jo J, Kilimnik G, Wojcik P, Hara M: Islet architecture: A comparative study. *Islets* 2009;1:129-136
4. von Mach MA, Schlosser J, Weiland M, Feilen PJ, Ringel M, Hengstler JG, Weilemann LS, Beyer J, Kann P, Schneider S: Size of pancreatic islets of Langerhans: a key parameter for viability after cryopreservation. *Acta Diabetol* 2003;40:123-129
5. Kilimnik G, Jo J, Perival V, Zielinski MC, Hara M: Quantification of islet size and architecture. *Islets* 2012;4:167-172
6. Virostko J, Powers AC: Molecular imaging of the pancreas in small animal models. *Gastroenterology* 2009;136:407-409
7. Paulus MJ, Gleason SS, Easterly ME, Foltz CJ: A review of high-resolution X-ray computed tomography and other imaging modalities for small animal research. *Lab Anim (NY)* 2001;30:36-45
8. Au C, Benedetto A, Aschner M: Manganese transport in eukaryotes: the role of DMT1. *Neurotoxicology* 2008;29:569-576
9. Silva AC, Lee JH, Aoki I, Koretsky AP: Manganese-enhanced magnetic resonance imaging (MEMRI): methodological and practical considerations. *NMR Biomed* 2004;17:532-543
10. Antkowiak PF, Stevens BK, Nunemaker CS, McDuffie M, Epstein FH: Manganese-enhanced magnetic resonance imaging detects declining pancreatic beta-cell mass in a cyclophosphamide-accelerated mouse model of type 1 diabetes. *Diabetes* 2013;62:44-48
11. Antkowiak PF, Tersey SA, Carter JD, Vandsburger MH, Nadler JL, Epstein FH, Mirmira RG: Noninvasive assessment of pancreatic beta-cell function in vivo with manganese-enhanced magnetic resonance imaging. *Am J Physiol Endocrinol Metab* 2009;296:E573-578
12. Antkowiak PF, Vandsburger MH, Epstein FH: Quantitative pancreatic β cell MRI using manganese-enhanced Look-Locker imaging and two-site water exchange analysis. *Magn Reson Med* 2012;67:1730-1739
13. Lamprianou S, Immonen R, Nabuurs C, Gjinovci A, Vinet L, Montet XC, Gruetter R, Meda P: High-resolution magnetic resonance imaging quantitatively detects individual pancreatic islets. *Diabetes* 2011;60:2853-2860
14. Rorsman P, Berggren PO, Hellman B: Manganese accumulation in pancreatic beta-cells and its stimulation by glucose. *Biochem J* 1982;202:435-444
15. Rorsman P, Hellman B: The interaction between manganese and calcium fluxes in pancreatic β -cells. *Biochem J* 1983;210:307-314
16. Crossgrove J, Zheng W: Manganese toxicity upon overexposure. *NMR Biomed* 2004;17:544-553
17. Lenzen S: The mechanisms of alloxan-and streptozotocin-induced diabetes. *Diabetologia* 2008;51:216-226
18. Tanaka K, Kawano T, Tomino T, Kawano H, Okada T, Oshita S, Takahashi A, Nakaya Y: Mechanisms of impaired glucose tolerance and insulin secretion during isoflurane anesthesia. *Anesthesiology* 2009;111:1044-1051
19. Desborough JP, Jones PM, Persaud SJ, Landon MJ, Howell SL: Isoflurane inhibits insulin secretion from isolated rat pancreatic islets of Langerhans. *Br J Anaesth* 1993;71:873-876
20. Lucaciu CM, Dragu C, Copaescu L, Morariu VV: Manganese transport through human erythrocyte membranes. An EPR study. *Biochim Biophys Acta* 1997;1328:90-98
21. Shibuya I, Douglas WW: Calcium channels in rat melanotrophs are permeable to manganese, cobalt, cadmium, and lanthanum, but not to nickel: evidence provided by fluorescence changes in fura-2-loaded cells. *Endocrinology* 1992;131:1936-1941
22. Irls E, Neco P, Lluesma M, Villar-Pazos S, Santos-Silva JC, Vettorazzi JF, Alonso-Magdalena P, Carneiro EM, Boschero AC, Nadal A, Quesada I: Enhanced glucose-induced intracellular signaling promotes insulin hypersecretion: pancreatic beta-cell functional adaptations in a model of genetic obesity and prediabetes. *Mol Cell Endocrinol* 2015;404:46-55
23. Merrins MJ, Poudel C, McKenna JP, Ha J, Sherman A, Bertram R, Satin LS: Phase Analysis of Metabolic Oscillations and Membrane Potential in Pancreatic Islet beta-Cells. *Biophys J* 2016;110:691-699
24. Weir GC, Bonner-Weir S: Five stages of evolving beta-cell dysfunction during progression to diabetes. *Diabetes* 2004;53 Suppl 3:S16-21
25. Atwater I, Dawson C, Scott A, Eddlestone G, Rojas E: The nature of the oscillatory behaviour in electrical activity from pancreatic beta-cell. *Horm Metab Res* 1979:100-107

26. Gimi B, Leoni L, Oberholzer J, Braun M, Avila J, Wang Y, Desai T, Philipson LH, Magin RL, Roman BB: Functional MR microimaging of pancreatic beta-cell activation. *Cell Transplant* 2006;15:195-203
27. Prentki M, Matschinsky FM, Madiraju SR: Metabolic signaling in fuel-induced insulin secretion. *Cell Metab* 2013;18:162-185
28. Bock T, Pakkenberg B, Buschard K: Increased islet volume but unchanged islet number in ob/ob mice. *Diabetes* 2003;52:1716-1722
29. Golson ML, Misfeldt AA, Kopsombut UG, Petersen CP, Gannon M: High Fat Diet Regulation of beta-Cell Proliferation and beta-Cell Mass. *Open Endocrinol J* 2010;4
30. Ha J, Satin LS, Sherman AS: A Mathematical Model of the Pathogenesis, Prevention, and Reversal of Type 2 Diabetes. *Endocrinology* 2016;157:624-635
31. Couri CE, Oliveira MC, Stracieri AB, Moraes DA, Pieroni F, Barros GM, Madeira MI, Malmegrim KC, Foss-Freitas MC, Simoes BP, Martinez EZ, Foss MC, Burt RK, Voltarelli JC: C-peptide levels and insulin independence following autologous nonmyeloablative hematopoietic stem cell transplantation in newly diagnosed type 1 diabetes mellitus. *JAMA* 2009;301:1573-1579
32. Voltarelli JC, Couri CE, Stracieri AB, Oliveira MC, Moraes DA, Pieroni F, Coutinho M, Malmegrim KC, Foss-Freitas MC, Simoes BP, Foss MC, Squiers E, Burt RK: Autologous nonmyeloablative hematopoietic stem cell transplantation in newly diagnosed type 1 diabetes mellitus. *JAMA* 2007;297:1568-1576
33. Atkins HL, Som P, Fairchild RG, Hui J, Schachner E, Goldman A, Ku T: Myocardial positron tomography with manganese-52m. *Radiology* 1979;133:769-774
34. Erlandsson K, Buvat I, Pretorius PH, Thomas BA, Hutton BF: A review of partial volume correction techniques for emission tomography and their applications in neurology, cardiology and oncology. *Phys Med Biol* 2012;57:R119-159
35. Gargiulo S, Greco A, Gramanzini M, Petretta MP, Ferro A, Larobina M, Panico M, Brunetti A, Cuocolo A: PET/CT imaging in mouse models of myocardial ischemia. *J Biomed Biotechnol* 2012;2012:541872
36. Eriksson O, Jahan M, Johnström P, Korsgren O, Sundin A, Halldin C, Johansson L: In vivo and in vitro characterization of [18 F]-FE-(+)-DTBZ as a tracer for beta-cell mass. *Nucl Med Bio* 2010;37:357-363
37. Kung M-P, Hou C, Lieberman BP, Oya S, Ponde DE, Blankemeyer E, Skovronsky D, Kilbourn MR, Kung HF: In vivo imaging of β -cell mass in rats using 18F-FP-(+)-DTBZ: a potential PET ligand for studying diabetes mellitus. *J Nucl Med* 2008;49:1171-1176
38. Simpson NR, Souza F, Witkowski P, Maffei A, Raffo A, Herron A, Kilbourn M, Jurewicz A, Herold K, Liu E: Visualizing pancreatic β -cell mass with [11 C] DTBZ. *Nucl Med Bio* 2006;33:855-864
39. Singhal T, Ding YS, Weinzimmer D, Normandin MD, Labaree D, Ropchan J, Nabulsi N, Lin SF, Skaddan MB, Soeller WC, Huang Y, Carson RE, Treadway JL, Cline GW: Pancreatic beta cell mass PET imaging and quantification with [11C]DTBZ and [18F]FP-(+)-DTBZ in rodent models of diabetes. *Mol Imaging Biol* 2011;13:973-984
40. Schafer MK, Hartwig NR, Kalmbach N, Klietz M, Anlauf M, Eiden LE, Weihe E: Species-specific vesicular monoamine transporter 2 (VMAT2) expression in mammalian pancreatic beta cells: implications for optimising radioligand-based human beta cell mass (BCM) imaging in animal models. *Diabetologia* 2013;56:1047-1056
41. Murthy R, Harris P, Simpson N, Van Heertum R, Leibel R, Mann JJ, Parsey R: Whole body [11C]-dihydrotrabenazine imaging of baboons: biodistribution and human radiation dosimetry estimates. *Eur J Nucl Med Mol Imaging* 2008;35:790-797
42. Moore A: Advances in beta-cell imaging. *Eur J Radiol* 2009;70:254-257
43. Di Galleonardo V, Signore A, Scheerstra EA, Visser AK, van Waarde A, Dierckx RA, de Vries EF: 11C-hydroxytryptophan uptake and metabolism in endocrine and exocrine pancreas. *J Nucl Med* 2012;53:1755-1763
44. Eriksson O, Espes D, Selvaraju RK, Jansson E, Antoni G, Sorensen J, Lubberink M, Biglarnia AR, Eriksson JW, Sundin A, Ahlstrom H, Eriksson B, Johansson L, Carlsson PO, Korsgren O: Positron emission tomography ligand [11C]5-hydroxy-tryptophan can be used as a surrogate marker for the human endocrine pancreas. *Diabetes* 2014;63:3428-3437
45. Carlbom L, Espes D, Lubberink M, Martinell M, Johansson L, Ahlstrom H, Carlsson PO, Korsgren O, Eriksson O: [11C]5-Hydroxy-Tryptophan PET for Assessment of Islet Mass During Progression of Type 2 Diabetes. *Diabetes* 2017;
46. Brom M, Woliner-Van Der Weg W, Joosten L, Frielink C, Bouckennooghe T, Rijken P, Andralojc K, Göke BJ, de Jong M, Eizirik DL: Non-invasive quantification of the beta cell mass by SPECT with 111In-labelled exendin. *Diabetologia* 2014;57:950-959
47. Kiesewetter DO, Gao H, Ma Y, Niu G, Quan Q, Guo N, Chen X: 18F-radiolabeled analogs of exendin-4 for PET imaging of GLP-1 in insulinoma. *Eur J Nucl Med Mol Imaging* 2012;39:463-473

48. Kirsi M, Cheng-Bin Y, Veronica F, Tamiko I, Viki-Veikko E, Johan R, Jori J, Tiina S, Tuula T, Marko T: ⁶⁴Cu- and ⁶⁸Ga-labelled [Nle14, Lys40 (Ahx-NODAGA) NH₂]-exendin-4 for pancreatic beta cell imaging in rats. *Mol Imaging Biol* 2014;16:255-263
49. Selvaraju RK, Velikyan I, Johansson L, Wu Z, Todorov I, Shively J, Kandeel F, Korsgren O, Eriksson O: In vivo imaging of the glucagonlike peptide 1 receptor in the pancreas with ⁶⁸Ga-labeled DO3A-exendin-4. *J Nucl Med* 2013;54:1458-1463
50. Wu Z, Todorov I, Li L, Bading JR, Li Z, Nair I, Ishiyama K, Colcher D, Conti PE, Fraser SE, Shively JE, Kandeel F: In vivo imaging of transplanted islets with ⁶⁴Cu-DO3A-VS-Cys40-Exendin-4 by targeting GLP-1 receptor. *Bioconjug Chem* 2011;22:1587-1594
51. Tornehave D, Kristensen P, Romer J, Knudsen LB, Heller RS: Expression of the GLP-1 receptor in mouse, rat, and human pancreas. *J Histochem Cytochem* 2008;56:841-851
52. Bandara N, Zheleznyak A, Cherukuri K, Griffith DA, Limberakis C, Tess DA, Jianqing C, Waterhouse R, Lapi SE: Evaluation of Cu-64 and Ga-68 Radiolabeled Glucagon-Like Peptide-1 Receptor Agonists as PET Tracers for Pancreatic β cell Imaging. *Mol Imaging Biol* 2016;18:90-98
53. Eter WA, Bos D, Frielink C, Boerman OC, Brom M, Gotthardt M: Graft revascularization is essential for non-invasive monitoring of transplanted islets with radiolabeled exendin. *Sci Rep* 2015;5
54. Paty BW, Bonner-Weir S, Laughlin MR, McEwan AJ, Shapiro AM: Toward development of imaging modalities for islets after transplantation: insights from the National Institutes of Health Workshop on Beta Cell Imaging. *Transplantation* 2004;77:1133-1137
55. Vegas AJ, Veisoh O, Gürtler M, Millman JR, Pagliuca FW, Bader AR, Doloff JC, Li J, Chen M, Olejnik K: Long-term glycemic control using polymer-encapsulated human stem cell-derived beta cells in immune-competent mice. *Nat Med* 2016;
56. Gotthardt M, Eizirik DL, Cnop M, Brom M: Beta cell imaging - a key tool in optimized diabetes prevention and treatment. *Trends Endocrinol Metab* 2014;25:375-377

Figure Legends

Figure 1. Tissue distribution and pharmacokinetics of $^{52}\text{Mn}^{2+}$. (A) Serial PET images of ICR mice injected intravenously with $^{52}\text{Mn}^{2+}$ (no anesthesia except during the PET scans). Coronal PET image slices were selected to best show pancreatic uptake. Arrows point to: P, pancreas; H, heart; L, liver; I, intestines; and SG, salivary gland. (B) ROI-based quantification of $^{52}\text{Mn}^{2+}$ uptake in the heart, liver, kidneys, muscle, pancreas, and submandibular salivary gland. (C) *Ex vivo* $^{52}\text{Mn}^{2+}$ biodistribution of euthanized mice following last time-point PET scans, determined by gamma counting. $n = 4$.

Figure 2. Rapid kinetics of tissue $^{52}\text{Mn}^{2+}$ uptake revealed by single IV bolus injection or continuous IV infusion. Dynamic PET time-activity curves (TACs) derived from hand-drawn ROIs for the pancreas, heart/blood, liver, kidneys, salivary gland, and muscle. Blue curves indicate TACs in mice injected with a rapid IV bolus of $^{52}\text{Mn}^{2+}$, while red curves indicate an IV infusion of $^{52}\text{Mn}^{2+}$ over the first 30 min of the scans.

Figure 3. Pharmacological manipulation of VDCC in isolated islets. (A) Cartoon of the β -cell triggering pathway. Molecular structures in blue indicate compounds that activate Ca^{2+} influx through VDCC, while compounds in red are inhibitory. (B) Uptake of $^{52}\text{Mn}^{2+}$ by isolated *ob/ob* mouse islets. Groups of 50 islets from 3 preparations were incubated with $^{52}\text{Mn}^{2+}$ (370 kBq) in the presence of glucose and VDCC modulators as indicated. Mean \pm S.D. *, $P < 0.05$; **, $P < 0.01$; ***, $P < 0.001$.

Figure 4. *In vivo* assessment of functional β -cell mass by $^{52}\text{Mn}^{2+}$ -PET. (A) Coronal PET images at 1 h post-injection showing the pancreas of ICR mice given IP injections of diazoxide (20 mg/kg), nifedipine (20 mg/kg), or glibenclamide (5 mg/kg) prior to the administration of a $^{52}\text{Mn}^{2+}$ rapid bolus. The pancreas (P) is demarcated by white dashed contours. (B) Manual ROI-based quantification of $^{52}\text{Mn}^{2+}$ uptake in various tissues from static PET images acquired at 1 h post-injection. (C) *Ex vivo* biodistribution analysis following PET imaging at 1 h post-injection. Significantly reduced pancreatic uptake of $^{52}\text{Mn}^{2+}$ is observed in mice that received nifedipine and diazoxide prior to radiotracer administration. Mice which received glibenclamide (5 mg/kg) prior to radiotracer administration had significantly higher pancreatic

uptake of $^{52}\text{Mn}^{2+}$ than the control mice, based on both PET imaging ($P = 0.02$) and biodistribution ($P = 0.047$) studies. Mean \pm S.D.; $n = 3-4$ mice per group. ***, $P < 0.001$.

Figure 5. $^{52}\text{Mn}^{2+}$ -PET imaging in streptozotocin (STZ)-induced type 1 diabetes. (A) Following the administration of an acute dose of STZ (180 mg/kg), ICR mice started to show symptoms of diabetes: reduced body weight and high blood glucose level (BGL; > 250 mg/dL). (B) One-hour post-injection coronal PET images of healthy (left panel) or diabetic (center/right panels) ICR mice showing clearly reduced PET signal in the pancreas of the STZ-diabetic mice. The significant decline in $^{52}\text{Mn}^{2+}$ uptake in the pancreas of STZ-diabetic mice was confirmed quantitatively by (C) ROI analysis of the PET images and (D) *ex vivo* biodistribution ($n = 3$ mice/group). (E) Quantification of β -cell mass for control and STZ-treated ICR mice. Data are shown as the mean \pm S.D.; $n = 4$ mice per group. *, $P < 0.05$, ***, $P < 0.001$.

Figure 6. $^{52}\text{Mn}^{2+}$ PET imaging in the *ob/ob* model of pre-type 2 diabetes. (A) Coronal PET images acquired at 1 h after $^{52}\text{Mn}^{2+}$ administration in *ob/ob* mice and C57BL/6J controls. The pancreas (P) is demarcated by white dashed contours. (B) Image-derived quantification expressed as SUV indicated a significant difference in $^{52}\text{Mn}^{2+}$ pancreatic uptake between groups (mean \pm S.D.; $n = 3$). (C) Quantification of β -cell mass for wildtype and *ob/ob* mice. $n = 3$ mice per group. (D) Recordings of islet Ca^{2+} in response to glucose (10 mM and 7 mM) from wildtype and *ob/ob* C57BL/6J mice. (E) Contingency plot showing the range of islet behaviors at each glucose level. (F) The oscillatory plateau fraction, reflecting the plasma membrane glucose sensitivity, was calculated as the fraction of time spent in the active state during each oscillation at 10 mM glucose. C57BL/6J, $n = 141$ islets from 4 mice; *ob/ob*, $n = 126$ islets from 4 mice. Results reflect mean \pm S.D. *, $P < 0.05$, **, $P < 0.01$, ***, $P < 0.001$, ****, $P < 0.0001$.

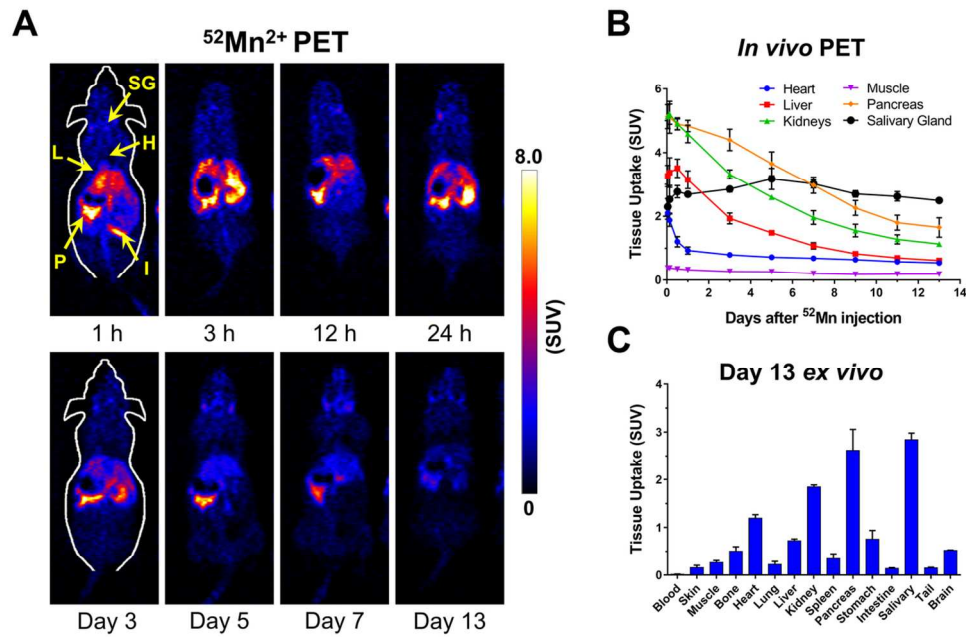


Figure 1. Tissue distribution and pharmacokinetics of $^{52}\text{Mn}^{2+}$. (A) Serial PET images of ICR mice injected intravenously with $^{52}\text{Mn}^{2+}$ (no anesthesia except during the PET scans). Coronal PET image slices were selected to best show pancreatic uptake. Arrows point to: P, pancreas; H, heart; L, liver; I, intestines; and SG, salivary gland. (B) ROI-based quantification of $^{52}\text{Mn}^{2+}$ uptake in the heart, liver, kidneys, muscle, pancreas, and submandibular salivary gland. (C) *Ex vivo* $^{52}\text{Mn}^{2+}$ biodistribution of euthanized mice following last time-point PET scans, determined by gamma counting. $n = 4$.

117x77mm (300 x 300 DPI)

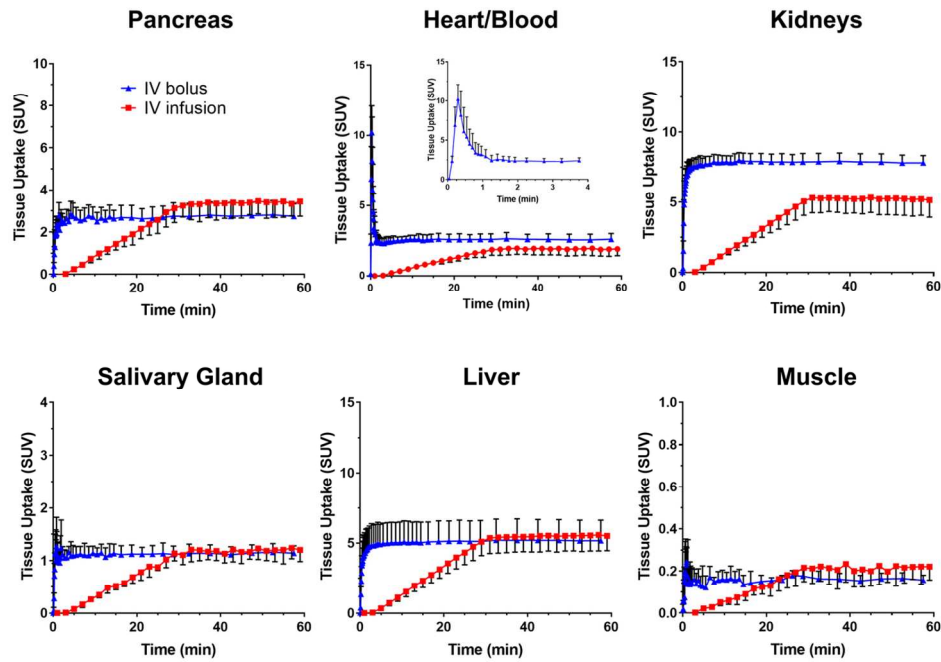


Figure 2. Rapid kinetics of tissue $^{52}\text{Mn}^{2+}$ uptake revealed by single IV bolus injection or continuous IV infusion. Dynamic PET time-activity curves (TACs) derived from hand-drawn ROIs for the pancreas, heart/blood, liver, kidneys, salivary gland, and muscle. Blue curves indicate TACs in mice injected with a rapid IV bolus of $^{52}\text{Mn}^{2+}$, while red curves indicate an IV infusion of $^{52}\text{Mn}^{2+}$ over the first 30 min of the scans.

122x83mm (300 x 300 DPI)

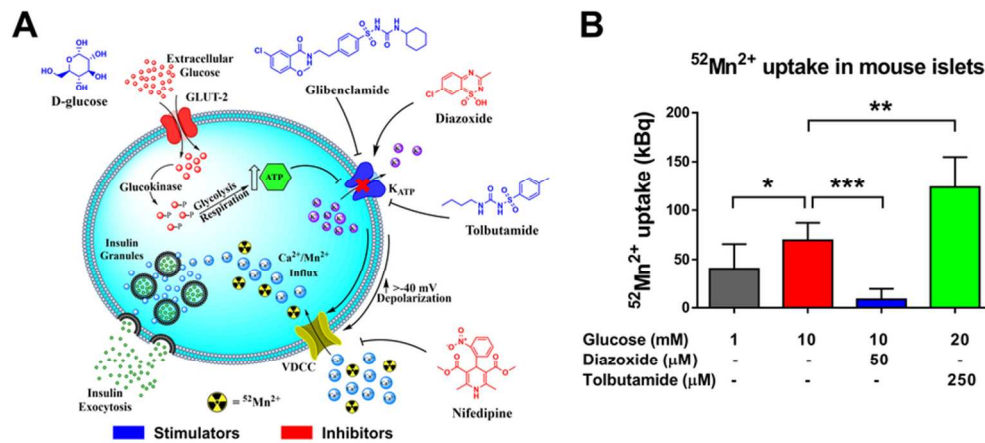


Figure 3. Pharmacological manipulation of VDCC in isolated islets. (A) Cartoon of the β -cell triggering pathway. Molecular structures in blue indicate compounds that activate Ca^{2+} influx through VDCC, while compounds in red are inhibitory. (B) Uptake of $^{52}\text{Mn}^{2+}$ by isolated *ob/ob* mouse islets. Groups of 50 islets from 3 preparations were incubated with $^{52}\text{Mn}^{2+}$ (370 kBq) in the presence of glucose and VDCC modulators as indicated. Mean \pm S.D. *, $P < 0.05$; **, $P < 0.01$; ***, $P < 0.001$.

80x36mm (300 x 300 DPI)

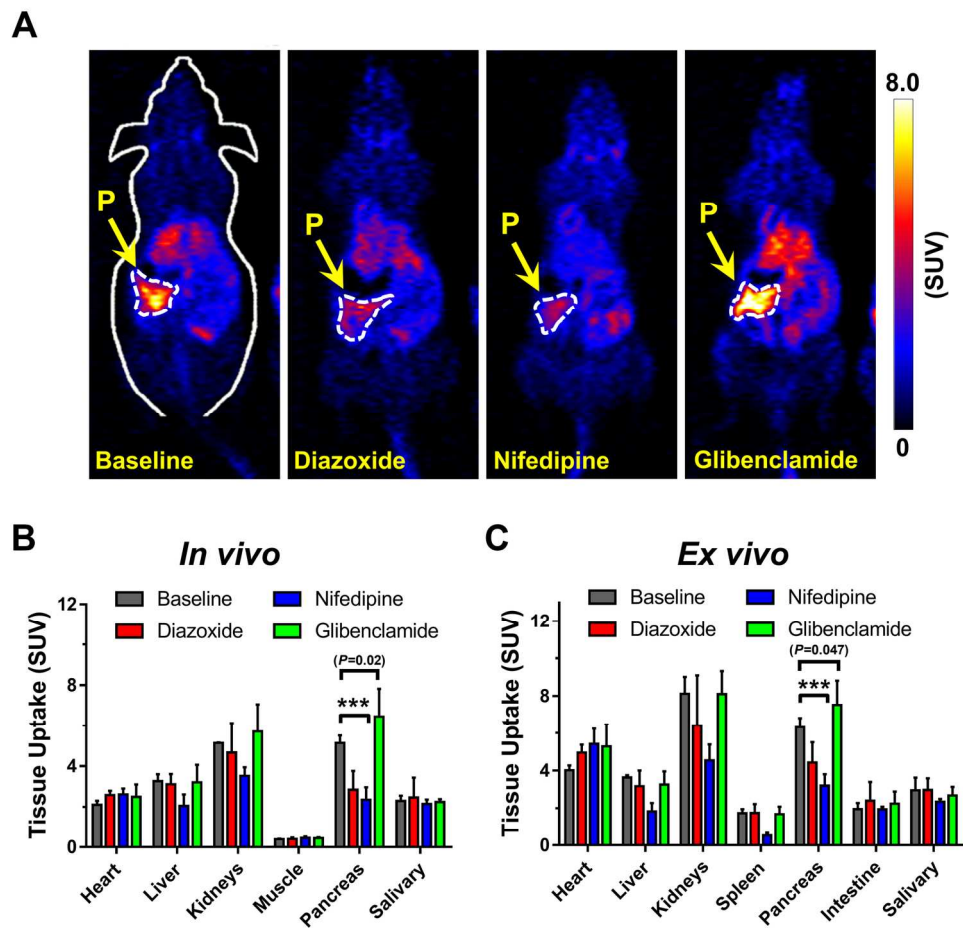


Figure 4. In vivo assessment of functional β -cell mass by $^{52}\text{Mn}^{2+}$ -PET. (A) Coronal PET images at 1 h post-injection showing the pancreas of ICR mice given IP injections of diazoxide (20 mg/kg), nifedipine (20 mg/kg), or glibenclamide (5 mg/kg) prior to the administration of a $^{52}\text{Mn}^{2+}$ rapid bolus. The pancreas (P) is demarcated by white dashed contours. (B) Manual ROI-based quantification of $^{52}\text{Mn}^{2+}$ uptake in various tissues from static PET images acquired at 1 h post-injection. (C) Ex vivo biodistribution analysis following PET imaging at 1 h post-injection. Significantly reduced pancreatic uptake of $^{52}\text{Mn}^{2+}$ is observed in mice that received nifedipine and diazoxide prior to radiotracer administration. Mice which received glibenclamide (5 mg/kg) prior to radiotracer administration had significantly higher pancreatic uptake of $^{52}\text{Mn}^{2+}$ than the control mice, based on both PET imaging ($P = 0.02$) and biodistribution ($P = 0.047$) studies. Mean \pm S.D.; $n = 3$ -4 mice per group. ***, $P < 0.001$.

166x155mm (300 x 300 DPI)

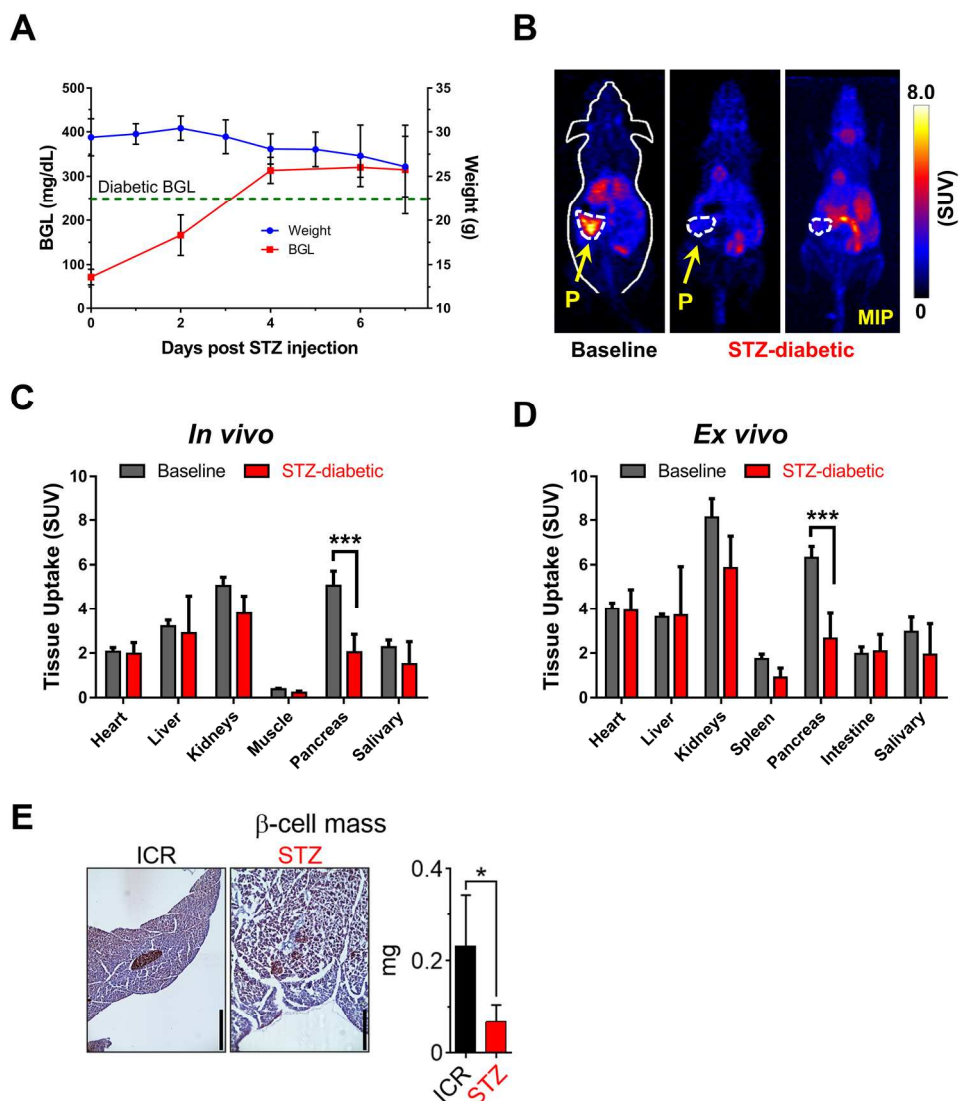


Figure 5. $^{52}\text{Mn}^{2+}$ -PET imaging in streptozotocin (STZ)-induced type 1 diabetes. (A) Following the administration of an acute dose of STZ (180 mg/kg), ICR mice started to show symptoms of diabetes: reduced body weight and high blood glucose level (BGL; > 250 mg/dL). (B) One-hour post-injection coronal PET images of healthy (left panel) or diabetic (center/right panels) ICR mice showing clearly reduced PET signal in the pancreas of the STZ-diabetic mice. The significant decline in $^{52}\text{Mn}^{2+}$ uptake in the pancreas of STZ-diabetic mice was confirmed quantitatively by (C) ROI analysis of the PET images and (D) ex vivo biodistribution (n = 3 mice/group). (E) Quantification of β -cell mass for control and STZ-treated ICR mice. Data are shown as the mean \pm S.D.; n = 4 mice per group. *, P < 0.05, ***, P < 0.001.

199x222mm (300 x 300 DPI)

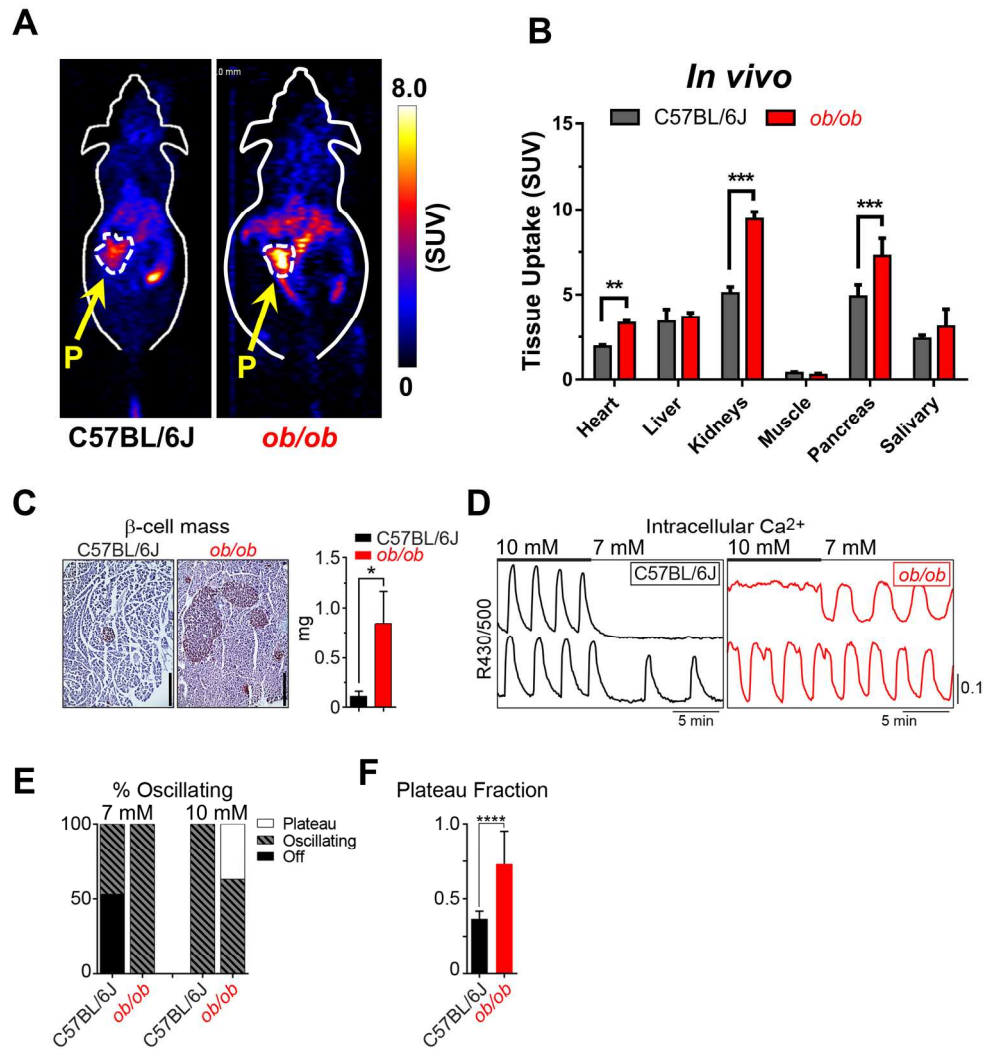


Figure 6. $^{52}\text{Mn}^{2+}$ -PET imaging in the *ob/ob* model of pre-type 2 diabetes. (A) Coronal PET images acquired at 1 h after $^{52}\text{Mn}^{2+}$ administration in *ob/ob* mice and C57BL/6J controls. The pancreas (P) is demarcated by white dashed contours. (B) Image-derived quantification expressed as SUV indicated a significant difference in $^{52}\text{Mn}^{2+}$ pancreatic uptake between groups (mean \pm S.D; $n = 3$). (C) Quantification of β -cell mass for wildtype and *ob/ob* mice. $n = 3$ mice per group. (D) Recordings of islet Ca^{2+} in response to glucose (10 mM and 7 mM) from wildtype and *ob/ob* C57BL/6J mice. (E) Contingency plot showing the range of islet behaviors at each glucose level. (F) The oscillatory plateau fraction, reflecting the plasma membrane glucose sensitivity, was calculated as the fraction of time spent in the active state during each oscillation at 10 mM glucose. C57BL/6J, $n = 141$ islets from 4 mice; *ob/ob*, $n = 126$ islets from 4 mice. Results reflect mean \pm S.D. *, $P < 0.05$, **, $P < 0.01$, ***, $P < 0.001$, ****, $P < 0.0001$.

189x200mm (300 x 300 DPI)

Supplementary Information

Radiomanganese PET Detects Changes in Functional β -cell Mass in Mouse Models of Diabetes

Reinier Hernandez,¹ Stephen A. Graves,¹ Trillian Gregg,^{2,3} Halena R. VanDeusen,² Rachel J. Fenske,² Haley N. Wienkes,² Christopher G. England,¹ Hector F. Valdovinos,¹ Justin J. Jeffery,⁴ Todd. E Barnhart,¹ Gregory W. Severin,^{5,6} Robert J. Nickles,¹ Michelle E. Kimple,^{2,7} Matthew J. Merrins,^{2,7,8} and Weibo Cai^{1,4,9}

¹Department of Medical Physics, University of Wisconsin-Madison, Madison, WI, USA, ²Department of Medicine, Division of Endocrinology, Diabetes & Metabolism, University of Wisconsin-Madison, Madison, WI, USA, ³Program in Biophysics, University of Wisconsin-Madison, Madison, WI, USA, ⁴Carbone Cancer Center, University of Wisconsin-Madison, Madison, WI, USA, ⁵Center for Nuclear Technologies, Technical University of Denmark, 4000 Roskilde, Denmark, ⁶Department of Chemistry, Michigan State University, East Lansing, MI, USA, ⁷William S. Middleton Memorial Veterans Hospital, Madison, WI, USA, ⁸Department of Biomolecular Chemistry, University of Wisconsin-Madison, Madison, WI, USA, ⁹Department of Radiology, University of Wisconsin-Madison, Madison, WI, USA.

Corresponding authors: Matthew J. Merrins, merrins@wisc.edu, and Weibo Cai, wcai@uwhealth.org.

Short title: $^{52}\text{Mn}^{2+}$ -PET imaging of functional β -cell mass in vivo

Authorship note: R.H. and S.A.G. contributed equally to this work.

Conflict of interest: The authors declare that no conflict of interest exists.

Mice

All animal experiments were approved by the Institutional Animal Care and Use Committees of the University of Wisconsin-Madison and the William S. Middleton Memorial Veterans Hospital. Male ICR (Envigo) and C57BL/6J wildtype and *ob/ob* mice (The Jackson Laboratory) were employed in this work. All mice were approximately ten weeks of age at the time of the experiments. Mice had access to food and water *ad libitum*, except under fasting condition when access to food was restricted for 6-12 hours.

⁵²Mn²⁺ Production

⁵²Mn²⁺ was produced as previously described (1). Production yields of up to 5.92 MBq/μAh (355 MBq/h @ 60 μA) were achieved using a chromium pellet pressed into a silver disc substrate. ⁵²Mn²⁺ was eluted in <1mL of 0.01 M NaOAc buffer (pH ~6.5) from a ~150 mg AG 1×8 column which had been conditioned with ethanol. As previously described (2), thin layer chromatographs confirmed the Mn²⁺ oxidation state following elution. End of bombardment radionuclidic purity was measured to be >99.5% by efficiency-calibrated high-purity germanium (HPGe) gamma spectrometry measurements. The only radionuclidic impurity observed was <0.5% of ⁵⁴Mn (t_{1/2}= 312.1 d), which does not decay by positron emission.

Islet Isolation

Mouse pancreatic islets were isolated by collagenase digestion as previously reported in (3). Briefly, mice were sacrificed via CO₂ asphyxiation followed by cervical dislocation. The common bile duct was perfused with 4 mL of an ice-cold solution containing type XI collagenase (0.5 mg/mL; Sigma Aldrich) and bovine serum albumin (BSA; 0.2 mg/mL; Sigma Aldrich) in Hank's Balanced Salt Solution (HBSS; Invitrogen). After inflation, the pancreas was removed to a glass vial containing 5 mL of collagenase solution, and incubated in a shaking water bath at 37°C for approximately 20 min. The digests were centrifuged at 50g for 2 min and islet pellets were washed three times with 30 mL ice-cold HBSS/BSA. The pellet was re-suspended and the islets were handpicked into 35 mm petri dishes. Following isolation, islets were placed in RPMI1640 media supplemented with penicillin (100 U/mL; Invitrogen), streptomycin (100 μg/mL; Invitrogen), and 10% (wt/vol) FBS (Sigma) and incubated overnight at 37°C in a 5% CO₂ atmosphere.

Pharmacological Disruption of $^{52}\text{Mn}^{2+}$ Uptake in Isolated Islets

Batches of 50 islets were transferred into 0.45 μm -filtered 1 mL centrifuge vials (Thermo Fisher Scientific), and incubated with 500 μL of Krebs-Ringer buffer (KRB: 118 mM NaCl, 5.4 mM KCl, 2.4 mM CaCl_2 , 1.2 mM MgSO_4 , 1 mM KH_2PO_3 , 20 mM HEPES; pH 7.4) containing 1 mM glucose for 30 min at 37°C. After removing the supernatant by centrifugation at 50g for 5 min, 250 μL of KRB containing 16.7 mM glucose, diazoxide (50 μM ; Tocris Biosciences), or tolbutamide (250 μM ; Selleckchem) were added, and the vials were spiked with 370 kBq (10 μCi) of $^{52}\text{Mn}^{2+}$. After 15 min of incubation, the islets were washed three times with KRB. $^{52}\text{Mn}^{2+}$ radioactivity in the islet pellets was quantified using an automated gamma counter (Perkin Elmer).

Ex vivo $^{52}\text{Mn}^{2+}$ Biodistribution Analysis

Ex vivo biodistribution studies were performed in all groups of mice to validate the results of $^{52}\text{Mn}^{2+}$ -PET imaging and obtain a more complete profile of tissue $^{52}\text{Mn}^{2+}$ uptake. Following the last imaging time point, mice were euthanized by CO_2 asphyxiation and 15 organs of interest were removed, wet-weighed, and counted in an automated gamma-counter (Wizard 2480, Perkin Elmer). The tissue uptake of $^{52}\text{Mn}^{2+}$ was reported as SUV (mean \pm S.D.).

Measurement of β -cell Mass

Similar as our previous report (4), mice were euthanized under anesthesia with CO_2 followed by cervical dislocation. The pancreas was immediately dissected, weighed, and fixed in 10% formalin on ice for 30 minutes. Pancreata were then washed in PBS and transferred through a series of solutions, beginning with 30% sucrose in PBS, 1:1 30% sucrose:OCT, and OCT before cryopreservation in OCT and storage at -80°C. 10-micron serial sections were cut on positively charged slides, with 9 sections per stop position (3/slide) and two stop positions per pancreas separated by at least 200 microns. For each pancreas, one slide per position was post-fixed, quenched of peroxidase activity with 3% H_2O_2 , and immunohistochemically labeled using guinea pig anti-insulin primary antibody (Dako A056401-2), diluted 1:500 in antibody diluent, and co-stained with hematoxylin (Sigma, GHS280). Slides were imaged using an automated pan-

and-stich microscope at 10× (Evos). β -cell fractional area was determined by quantifying the percent of insulin-positive pancreas area as a total of the full pancreas area for each section, followed by averaging of 2 distinct sections per mouse. Images were analyzed using ImageJ (64-bit) software (National Institutes of Health, Bethesda, MD) with shading correction. β -cell mass was calculated by multiplying β -cell fractional area by the pancreatic wet weight.

Islet Ca^{2+} Imaging

For measurements of cytosolic Ca^{2+} , islets were pre-incubated in 2.5 μM FuraRed (Molecular Probes) for 45 min at 37°C. Islets were then placed in an RC-41LP glass-bottomed chamber mounted in a QE-1 platform (Warner Instruments) on a Nikon Ti-Eclipse inverted microscope equipped with a 20×/0.75NA SuperFluor objective (Nikon Instruments). The chamber was perfused with standard external solution with glucose (in mM: 135 NaCl, 4.8 KCl, 5 CaCl₂, 1.2 MgCl₂, 20 HEPES; pH 7.35). The flow rate was 0.5 ml/min and temperature was maintained at 33°C using inline solution and chamber heaters (Warner Instruments). Excitation was provided by a SOLA SEII 365 (Lumencor) set to 10% output. Excitation (430/20 nm and 500/20 nm) and emission (630/70 nm) filters (ET type, Chroma Technology Corporation) were used in combination with an FF444/521/608-Di01 dichroic (Semrock). Fluorescence emission was collected with a Hamamatsu ORCA-Flash4.0 V2 Digital CMOS camera at 0.125 Hz. A single region of interest was used to quantify the average response of each islet as the excitation ratio (R430/500) using Nikon Elements and MathWorks MATLAB software as in (3).

Statistics

A minimum sample size of three (n=3) was used in all *in vitro* and *in vivo* experiments. The uptake of $^{52}\text{Mn}^{2+}$ in the different tissues was reported as SUV (mean \pm S.D.) and the differences between groups were evaluated for significance using a two-tailed Student's t-test. Differences were considered statistically significant at $P < 0.05$.

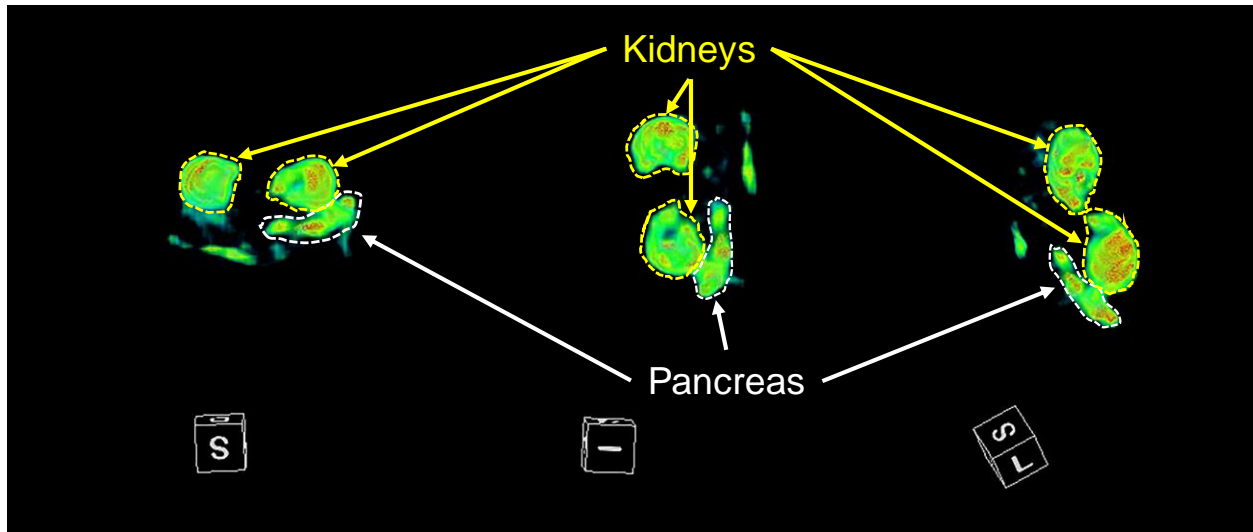


Figure S1 Three-dimensional rendering of the pancreas and kidneys PET signal in ICR mice injected a rapid IV $^{52}\text{Mn}^{2+}$ bolus. Three different view angles are presented showing the separation between pancreas and the left kidney. The animal subject shown here is the same displayed in Figure 1 of the main text.

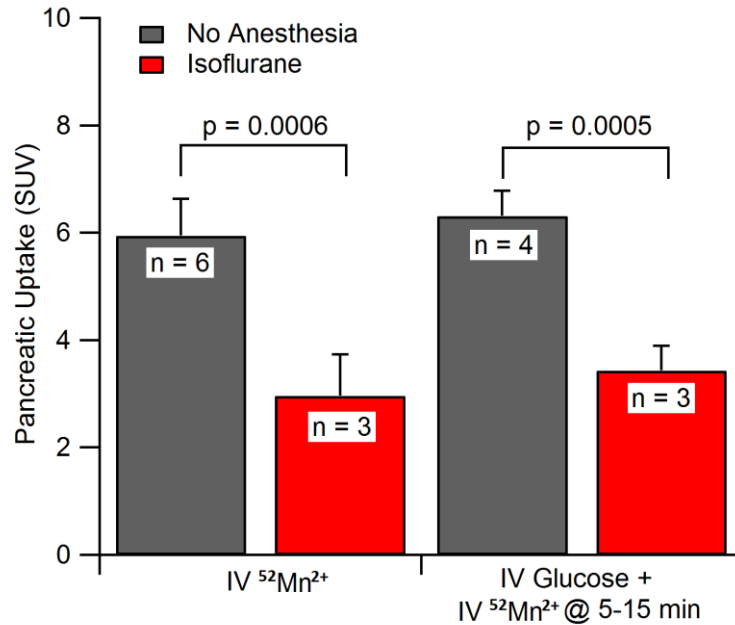


Figure S2. Impact of isoflurane on pancreatic uptake of $^{52}\text{Mn}^{2+}$ in mice. ICR mice (3-6 per group) received either an intravenous bolus of $^{52}\text{Mn}^{2+}$, or an intraperitoneal injection of glucose (1 mg/kg) followed by an intravenous infusion of $^{52}\text{Mn}^{2+}$ from 5 to 15 minutes following glucose administration. A subset of these treatments was anesthetized with 2% isoflurane during injections, whereas the rest of the mice were not anesthetized. One hour following $^{52}\text{Mn}^{2+}$ administration, mice were euthanized and *ex vivo* biodistribution studies were performed via gamma counting. Pancreatic uptake of $^{52}\text{Mn}^{2+}$ was found to be significantly lower in both groups under isoflurane anesthesia, when compared to non-anesthetized controls, suggesting that isoflurane prevents voltage-dependent calcium channel (VDCC) mediated $^{52}\text{Mn}^{2+}$ influx.

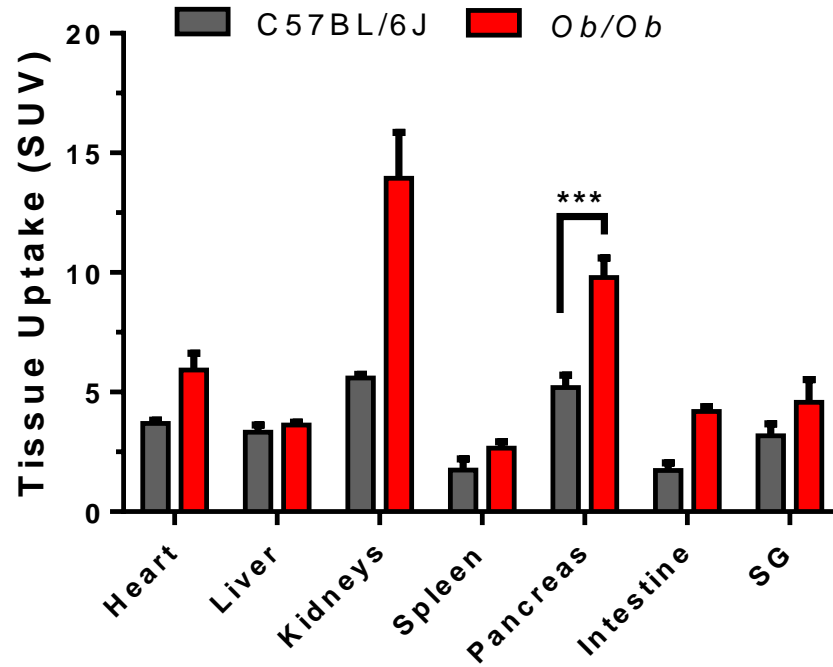


Figure S3 *Ex vivo* biodistribution of lean (C57BL/6J) and obese (ob/ob) mice, one-hour post injection of $^{52}\text{Mn}^{2+}$. Significantly higher $^{52}\text{Mn}^{2+}$ uptake can be noted in obese mice compared to the lean controls (***) $P < 0.0001$; $n=3$).

Table S1. Quantitative results of longitudinal PET imaging studies in ICR mice administered a $^{52}\text{Mn}^{2+}$ intravenous bolus (n = 4)

Time (days)	Organ/tissue uptake					
	Heart/blood	Liver	Kidneys	Muscle	Pancreas	S Gland
0.042	2.11 ± 0.20	3.27 ± 0.34	5.13 ± 0.02	0.38 ± 0.03	5.13 ± 0.37	2.30 ± 0.26
0.125	1.88 ± 0.19	3.37 ± 0.47	5.21 ± 0.32	0.38 ± 0.02	5.11 ± 0.50	2.53 ± 0.44
0.5	1.21 ± 0.16	3.51 ± 0.29	4.90 ± 0.19	0.35 ± 0.05	4.89 ± 0.17	2.77 ± 0.19
1	0.93 ± 0.11	3.15 ± 0.28	4.59 ± 0.27	0.33 ± 0.03	4.84 ± 0.18	2.69 ± 0.05
3	0.80 ± 0.08	1.94 ± 0.17	3.32 ± 0.14	0.27 ± 0.05	4.40 ± 0.34	2.85 ± 0.09
5	0.72 ± 0.05	1.49 ± 0.05	2.60 ± 0.03	0.26 ± 0.03	3.65 ± 0.37	3.18 ± 0.33
7	0.69 ± 0.00	1.08 ± 0.10	1.96 ± 0.21	0.20 ± 0.02	2.98 ± 0.25	3.02 ± 0.13
9	0.64 ± 0.02	0.83 ± 0.06	1.56 ± 0.20	0.18 ± 0.02	2.26 ± 0.23	2.70 ± 0.10
11	0.58 ± 0.03	0.70 ± 0.02	1.28 ± 0.14	0.19 ± 0.01	1.80 ± 0.23	2.63 ± 0.15
13	0.54 ± 0.03	0.62 ± 0.01	1.13 ± 0.06	0.19 ± 0.01	1.65 ± 0.31	2.50 ± 0.08

Mean ± SD values are reported as standardized uptake value (SUV)

Table S2. *Ex vivo* biodistribution of $^{52}\text{Mn}^{2+}$ at day 13 after intravenous administration in healthy ICR mice. n = 4.

Organ/tissue	$^{52}\text{Mn}^{2+}$ uptake (SUV)*	$^{52}\text{Mn}^{2+}$ uptake (%ID/g)*
Blood	0.01 ± 0.01	0.06 ± 0.02
Skin	0.16 ± 0.05	0.56 ± 0.18
Muscle	0.26 ± 0.04	0.93 ± 0.14
Bone	0.50 ± 0.09	1.78 ± 0.28
Heart	1.19 ± 0.08	4.25 ± 0.18
Lung	0.22 ± 0.06	0.80 ± 0.22
Liver	0.72 ± 0.04	2.57 ± 0.14
Kidney	1.85 ± 0.04	6.57 ± 0.23
Spleen	0.35 ± 0.10	1.23 ± 0.34
Pancreas	2.62 ± 0.44	9.30 ± 1.29
Stomach	0.76 ± 0.18	2.68 ± 0.61
Intestine	0.14 ± 0.02	0.49 ± 0.07
Salivary	2.84 ± 0.13	10.13 ± 0.38
Tail	0.14 ± 0.01	0.54 ± 0.05
Brain	0.52 ± 0.01	1.87 ± 0.07
*Mean ± SD		

Table S3. Quantitative results of PET imaging in ICR mice 1 h post administration of $^{52}\text{Mn}^{2+}$ under various conditions to stimulate or inhibit insulin release.

Organs	Baseline (n=3)	Diazoxide (n=3)	Nifedipine (n=3)	Glibenclamide (n=4)	STZ-diabetic (n=3)
Heart/blood	2.11 ± 0.20	2.58 ± 0.22	2.61 ± 0.30	2.50 ± 0.60	1.97 ± 0.50
Liver	3.27 ± 0.34	3.11 ± 0.50	2.06 ± 0.56	3.20 ± 0.87	2.89 ± 1.70
Kidneys	5.13 ± 0.02	4.66 ± 1.48	3.52 ± 0.43	5.70 ± 1.35	3.80 ± 0.78
Muscle	0.38 ± 0.03	0.40 ± 0.07	0.44 ± 0.07	0.44 ± 0.04	0.23 ± 0.06
Pancreas	5.13 ± 0.38	2.85 ± 0.92	2.36 ± 0.61	6.47 ± 1.36	2.04 ± 0.81
Salivary Gland	2.30 ± 0.26	2.46 ± 0.97	2.15 ± 0.22	2.25 ± 0.14	1.51 ± 1.01

Mean ± SD values are reported as standardized uptake value (SUV)

Table S4. One-hour post injection *ex vivo* biodistribution data in ICR mice administered $^{52}\text{Mn}^{2+}$ under various conditions to stimulate or inhibit insulin release.

Organs	Baseline (n=3)	Diazoxide (n=3)	Nifedipine (n=3)	Glibenclamide (n=4)	STZ diabetic (n=3)
Heart	4.01 ± 0.26	4.96 ± 0.46	5.42 ± 0.81	5.29 ± 1.19	1.97 ± 0.50
Liver	3.63 ± 0.13	3.17 ± 0.83	1.84 ± 0.45	3.26 ± 0.70	2.89 ± 1.70
Kidneys	8.12 ± 0.88	6.42 ± 2.67	4.55 ± 0.84	8.10 ± 1.22	3.80 ± 0.78
Spleen	1.74 ± 0.22	1.75 ± 0.47	0.52 ± 0.13	1.68 ± 0.40	0.23 ± 0.06
Pancreas	6.31 ± 0.51	4.43 ± 1.08	3.20 ± 0.61	7.53 ± 1.29	2.04 ± 0.81
Intestine	1.96 ± 0.32	2.40 ± 0.99	1.94 ± 0.14	2.25 ± 0.64	1.51 ± 1.01
Salivary Gland	2.90 ± 0.67	2.97 ± 0.62	2.35 ± 0.16	2.68 ± 0.46	1.97 ± 0.50

Mean ± SD values are reported as standardized uptake value (SUV)

Table S5. *In vivo* PET and *ex vivo* biodistribution data in C57BL/6J and obese (*ob/ob*) mice one-hour after intravenous administration of $^{52}\text{Mn}^{2+}$. n = 3.

Organs	<i>In vivo</i> PET Data		Organs	<i>Ex vivo</i> biodistribution	
	C57BL/6J (n=3)	<i>Ob/Ob</i> (n=3)		C57BL/6J (n=3)	<i>Ob/Ob</i> (n=3)
Heart/blood	1.93 ± 0.10	3.32 ± 0.13	Heart	3.68 ± 0.15	5.93 ± 0.69
Liver	3.40 ± 0.73	3.68 ± 0.25	Liver	3.33 ± 0.29	3.63 ± 0.10
Kidneys	5.08 ± 0.37	9.43 ± 0.44	Kidneys	5.58 ± 0.16	13.94 ± 1.91
Muscle	0.38 ± 0.06	0.26 ± 0.09	Spleen	1.74 ± 0.46	2.65 ± 0.27
Pancreas	4.89 ± 0.68	7.27 ± 1.03	Pancreas	5.19 ± 0.52	9.79 ± 0.83
Salivary Gland	2.40 ± 0.20	3.11 ± 1.05	Intestine	1.72 ± 0.33	4.17 ± 0.21
			Salivary Gland	3.18 ± 0.49	4.57 ± 0.95

Mean ± SD values are reported as standardized uptake value (SUV)

Table S6. Quantitative results of longitudinal PET imaging studies in ICR mice administered a $^{52}\text{Mn}^{2+}$ intravenous bolus (n = 4)

Time (days)	Organ/tissue uptake					
	Heart/blood	Liver	Kidneys	Muscle	Pancreas	S Gland
0.042	7.50 ± 0.61	11.63 ± 1.12	18.30 ± 0.53	1.37 ± 0.12	18.30 ± 1.71	8.20 ± 0.92
0.125	6.70 ± 0.62	12.00 ± 1.41	18.57 ± 1.42	1.37 ± 0.06	18.23 ± 2.21	9.00 ± 1.35
0.5	4.30 ± 0.61	12.50 ± 0.69	17.47 ± 0.21	1.27 ± 0.15	17.43 ± 0.87	9.87 ± 0.49
1	3.33 ± 0.42	11.20 ± 0.72	16.33 ± 0.72	1.17 ± 0.12	17.23 ± 0.40	9.60 ± 0.30
3	2.83 ± 0.21	6.90 ± 0.46	11.83 ± 0.45	0.96 ± 0.15	15.70 ± 1.59	10.17 ± 0.38
5	2.57 ± 0.15	5.30 ± 0.10	9.27 ± 0.25	0.93 ± 0.06	13.03 ± 1.56	11.20 ± 0.85
7	2.47 ± 0.06	3.83 ± 0.29	7.00 ± 0.87	0.73 ± 0.07	10.63 ± 1.17	10.77 ± 0.71
9	2.30 ± 0.10	2.93 ± 0.15	5.57 ± 0.84	0.64 ± 0.05	8.07 ± 0.90	9.63 ± 0.32
11	2.07 ± 0.15	2.50 ± 0.10	4.57 ± 0.61	0.66 ± 0.02	6.43 ± 0.95	9.37 ± 0.55
13	1.93 ± 0.06	2.20 ± 0.10	4.03 ± 0.31	0.66 ± 0.05	5.90 ± 1.20	8.90 ± 0.26

Mean ± SD values are reported as percent injected dose per gram (%ID/g)

Table S7. Quantitative results of PET imaging in ICR mice 1 h post administration of $^{52}\text{Mn}^{2+}$ under various conditions to stimulate or inhibit insulin release.

Organs	Baseline (n=3)	Diazoxide (n=3)	Nifedipine (n=3)	Glibenclamide (n=4)	STZ-diabetic (n=3)
Heart/blood	7.50±0.61	8.27±1.75	10.93±0.76	8.25±1.68	7.63±1.94
Liver	11.63±1.12	9.77±0.42	8.53±1.63	10.55±2.39	11.83±8.63
Kidneys	18.30±0.53	14.53±3.27	14.73±0.99	18.73±2.65	14.80±3.82
Muscle	1.37±0.12	1.29±0.37	1.83±0.15	1.45±0.10	0.86±0.14
Pancreas	18.30±1.71	9.03±2.74	9.87±2.42	21.28±2.43	7.70±2.49
Salivary Gland	8.20±0.92	7.97±3.69	9.03±1.10	7.48±0.29	5.53±3.20

Mean ± SD values are reported as standardized uptake value (%ID/g)

Table S8. One-hour post injection *ex vivo* biodistribution data in ICR mice administered $^{52}\text{Mn}^{2+}$ under various conditions to stimulate or inhibit insulin release.

Organs	Baseline (n=3)	Diazoxide (n=3)	Nifedipine (n=3)	Glibenclamide (n=4)	STZ diabetic (n=3)
Heart	13.10±1.90	15.85±3.02	22.72±3.12	17.46±3.10	15.13±3.33
Liver	8.01±0.33	9.87±1.62	7.63±1.24	10.79±2.22	15.11±11.18
Kidneys	30.77±4.67	19.92±6.50	19.04±3.15	26.85±3.34	22.85±6.62
Spleen	5.85±0.69	5.42±0.94	2.18±0.42	5.52±0.85	3.39±1.36
Pancreas	21.62±2.49	14.03±3.27	13.33±1.64	24.85±2.05	10.14±3.92
Intestine	9.23±0.74	7.44±2.56	8.17±0.69	7.55±2.58	8.33±4.19
Salivary Gland	10.03±1.78	8.81±3.80	9.86±0.83	8.85±0.63	7.11±4.45

Mean ± SD values are reported as percent injected dose per gram (%ID/g)

Table S9. *In vivo* PET and *ex vivo* biodistribution data in C57BL/6J and obese (*ob/ob*) mice one-hour after intravenous administration of $^{52}\text{Mn}^{2+}$. n = 3.

Organs	<i>In vivo</i> PET Data		Organs	<i>Ex vivo</i> biodistribution	
	C57BL/6J (n=3)	<i>Ob/Ob</i> (n=3)		C57BL/6J (n=3)	<i>Ob/Ob</i> (n=3)
Heart/blood	8.57±0.60	7.33±0.50	Heart	16.36±0.74	13.10±1.90
Liver	15.07±2.97	8.10±0.36	Liver	14.75±1.01	8.01±0.33
Kidneys	22.53±1.31	20.80±1.61	Kidneys	24.79±1.13	30.77±4.67
Muscle	1.70±0.30	0.58±0.20	Spleen	7.72±1.95	5.85±0.69
Pancreas	21.70±2.86	16.07±2.67	Pancreas	23.03±1.94	21.62±2.49
Salivary Gland	10.63±0.91	6.80±2.08	Intestine	7.62±1.42	9.23±0.74
			Salivary Gland	14.12±2.35	10.01±1.78

Mean ± SD values are reported as standardized uptake value (%ID/g)

REFERENCES

1. Graves SA, Hernandez R, Fonslet J, England CG, Valdovinos HF, Ellison PA, Barnhart TE, Elema DR, Theuer CP, Cai W: Novel Preparation Methods of ⁵²Mn for ImmunoPET Imaging. *Bioconjug Chem* 2015;26:2118-2124
2. Lewis CM, Graves SA, Hernandez R, Valdovinos HF, Barnhart TE, Cai W, Meyerand ME, Nickles RJ, Suzuki M: ⁵²Mn production for PET/MRI tracking of human stem cells expressing divalent metal transporter 1 (DMT1). *Theranostics* 2015;5:227
3. Gregg T, Poudel C, Schmidt BA, Dhillon RS, Sdao SM, Truchan NA, Baar EL, Fernandez LA, Denu JM, Eliceiri KW, Rogers JD, Kimple ME, Lamming DW, Merrins MJ: Pancreatic beta-Cells From Mice Offset Age-Associated Mitochondrial Deficiency With Reduced KATP Channel Activity. *Diabetes* 2016;65:2700-2710
4. Brill AL, Wisinski JA, Cadena MT, Thompson MF, Fenske RJ, Brar HK, Schaid MD, Pasker RL, Kimple ME: Synergy Between Galphaz Deficiency and GLP-1 Analog Treatment in Preserving Functional beta-Cell Mass in Experimental Diabetes. *Mol Endocrinol* 2016;30:543-556